Università degli Studi di Padova

DIPARTIMENTO DI FISICA E ASTRONOMIA "GALILEO GALILEI"

Corso di Laurea Magistrale in Fisica

Study for the development of a cavity enhanced single photon source

Laureando:
Elisa Da Ros
Matricola 1040073

Relatore:
Prof. Giovanni Mattei

Relatori esterni:
Prof. Jan W. Thomsen
University of Copenhagen, Denmark
Prof. Ulrik L. Andersen
Technical University of Denmark, Denmark

Anno Accademico 2014-2015

Contents

Acknowledgements

At first I gratefully acknowledge Prof. Giovanni Mattei for accepting me as his Master's candidate and enabling me to go to Copenhagen. I want to thank him also for his wise suggestions.

I would like to express my gratitude towards Prof. Ulrik L. Andersen for introducing me into this project and giving me the possibility to be part of his group.

I would like to give a special thanks to Jonas S. Neergaard-Nielsen for mentoring me along the project with his unending enthusiasm. His guidance and his encouragement have been fundamental in this work.

I would like to mention also all the other members of the QPIT group, Alex, Shailesh, Niels, Bo, Louise, Jörn, Adriano, Hugo, Amine, Christian, who welcomed me in a particularly friendly atmosphere. They have always been sympathetic and helpful, giving me valuable advices every time I had the chance to share lab time or conversations with them.

I am unspeakably grateful to all my friends in Italy and all over the world. In particular my time in graduate school would not have been the same without Ilaria, Laura, and Anna. They have cheered me up every time I needed preserving my mental health, we shared laughs and many other incredible moments.

A big thank you goes to my boyfriend Marco for all his support, encouragement and understanding.

Vorrei ringraziare infine i miei genitori e Francesco, grazie per esserci sempre stati, sempre disponibili ogni volta che ne ho avuto bisogno.

Chapter 1

Introduction

In the recent years an increased interest in quantum computation and quantum information has been driving the search for sources suitable to produce single quantum bits (qubits) [1, 2]. The idea to use a superposition of quantum states as basic elements for quantum computation and information is brilliant but technically demanding. Such qubits are required to hold information over time, therefore quantum decoherence represents a major challenge for the practical realization of quantum computers. One of the earliest proposals for quantum computation is based on implementing a quantum bit with two optical modes containing one single-photon [3].

Among the several techniques providing single photon sources, ion traps have been proven successful in creating entangled states in a deterministic fashion [4]. Another interesting approach involves the use of cold neutral atoms in high finesse optical cavities: neutral atoms show long decoherence times and are highly controllable using laser cooling technologies and magneto-optical traps [5].
Many experiments were then conducted aiming to understand the dynamics of a single atom in a cavity [6] and leading to efficient production of single-photon sources [8, 9]. In particular microstructured chip traps have been of great interest [10]. All these single-photon sources, however, present major challenges to their practical realization. They require high magnetic fields, state-of-the-art vacuum technology and cryogenic temperatures, resulting in bulky and complex systems to be implemented.

Alternatively, a nitrogen-vacancy (NV) color center in diamond is a solid state quantum system that has gathered much interest in the recent decades [11]. An NV center occurs in diamond when a substitutional nitrogen atom sits next to a missing carbon atom. The negatively charged state of this optically-active impurity forms a spin triplet which can implement a qubit. Additionally their spin information can be coupled to optical photons enabling transmission [12]. Decoherence times up to 3 ms have been demonstrated in isotopically-purified diamond [13]. This figure represents

an extremely long time for a solid-state quantum bit and therefore NV centers display a strong potential to provide practical single-photon sources.

Additionally, being solid state systems, NV centers do not require magnetic confinement, therefore enabling not only quantum computing [14] but also high-efficiency magnetometry [15]. These applications however require that the photons emitted from NV centers are harvested in a single mode with high efficiency. Consequently, a strong focus has been directed towards coupling the NV center to a microcavity mode [16] or a waveguide mode [18].

More interestingly, a single NV center located in nanodiamonds can be coupled to a fiber-based fiber Fabry-Pérot cavity (FFPC) [17] operated at room temperature. This cavity type consists of a plane dielectric mirror and an optical fiber facet which has been laser-machined to yield a concave imprint prior to deposition of a dielectric multilayer coating [19]. Surface processing with CO_2 laser at 10.6 μm ensures very smooth surfaces [20] for the fabrication of low-scatter micro-optical devices, resulting in high finesse optical cavities with small mode volumes. Furthermore, nanodiamonds containing NV centers can be spin-coated directly on the plane dielectric mirror. This device therefore has several advantages: the ultra-low loss mirror offers a high finesse cavity, the microscopic mode volume of the resonator allows achieving large Purcell factors and the NV emission is automatically fiber coupled, thus the single photon is efficiently extracted into a single mode.

This project has been carried out in the laboratory of the Technical University of Denmark, in the Quantum Physics and Information Technology group, under the supervision of Ulrik Lund Andersen and Jonas Schou Neergaard-Nielsen.

The aim of this work is to laser-machine fiber end facets with concave structures to make them suitable as resonator mirrors for high finesse cavity. The optical cavity taken into account for this project is a FFPC, which consists of a plane dielectric mirror onto which nanodiamonds are spin-coated and of single mode fiber facet machined to yield a concave imprint. The single-photon emission of excited NV centers in the nanodiamonds is enhanced by the cavity and collected through the single mode fiber. For this purpose a new experimental setup is assembled and characterized for the fabrication of concave structures on the micrometers scale. A further study is conducted about the impact of the parameters used in the laser-machining on the resonator properties: the resonator performances are predicted from the concave structures properties before applying a dielectric mirror coating.

This analysis requires also studies about the cavity alignment and the NV centers investigation.

Outline of this work

Chapter 2 introduces theoretically the basic concepts required in the project. At first the basic notions to describe the light field emitted by laser devices and confined into resonators are discussed.

A particular focus is directed towards Gaussian beams and their propagation. The cavity quantum electrodynamics is the subsequent topic. The key parameters that determine the properties of optical cavities are enunciated as well as the loss mechanisms controlling the decay of the light field. Different coupling regimes are defined for the interaction between the light field in the cavity and the electromagnetic emission of an atom coupled into the resonator. An introduction on NV centers in nanodiamonds is also provided. Finally the micro-fabrication to create concave features with ultra-low roughness in silica is described. The processing is based on strong absorption of 10.6 μm radiation provided by the CO_2 laser light.

Chapter 3 presents and characterize the setup implemented for the laser-machining of silica plates and fiber end faces with the CO_2 laser beam. The setup is assembled to fulfil requirements of power stability, management of the beam profile and accurate positioning. Beam profiling method and width measurements are compared to simulations of the beam size in the optical path. A shutter based on an Hard Disk Drive is inserted in setup: this shutter-type has proved fast switching. This device is therefore characterized to verify its suitability for the setup. Finally a LabView program, implemented for this experiment, controls the driving signals of different elements in the setup. The principles of this LabView routine are discussed.

Chapter 4 deals with the experimental results of laser-machining on silica plates and fiber tips. A set of concave structures is imprinted through laser ablation on silica plates and on fiber tips. These structures are then characterized using surface profilometry through atomic force microscope (AFM) and the impact of the laser parameters on the shape of the structures is investigated. This analysis is necessary to estimate the effectiveness of the depressions as resonators mirrors for a Fabry-Pérot cavity. As a consequence simulation of FFPC properties are carried out for resonator assemblies with laser-machined fiber tips subjected to high-performance dielectric coating, using the concave structures' features.

In Chapter 5 the realization of a macroscopic cavity tuned by a piezoelectric actuator is presented. Particular attention is given to the assembly of the setup and the cavity coupling with a laser diode. The stability conditions for the resonator are derived and estimations of the cavity finesse are compared to the expectations from theory. Furthermore the characterization of NV centers are carried out on a scanning confocal microscope. A Hanbury-Brown and Twiss setup is used to measure the second order correlation function of the light emitted by the NV centers, proving the single-photon emission.

Finally Chapter 6 summarizes the key results and it provides a brief outlook on the future developments of the findings presented.

Chapter 2

Theoretical foundation

In this chapter the theoretical foundation necessary to understand the topics that are going to be dealt with in the project is presented.

In Section 2.1 the principles of Gaussian beams are discussed, focusing on their propagation. Following, a general overview about optical cavities is provided in Section 2.2. The theory underlying nitrogen-vacancy centers is introduced in Section 2.3. Finally, in Section 2.4 the laser ablation process is analyzed.

2.1   Gaussian beams

In optics, a Gaussian beam is a beam that exhibits a transverse Gaussian intensity distribution of the electrical field localized near the propagation axis. The output light emitted by laser resonators and the light field inside an optical cavity can be described by a Gaussian beam model.

The variation of the electric field in a plane transverse to propagation direction of the beam characterizes the mode structure of the beam. The fundamental mode for a laser beam occurs when the electric field has the maximum intensity at the center of the beam and drops off with a Gaussian profile. The conventional notation used to describe the transverse mode of an electromagnetic field propagation along the z-axis is TEM_{mn}, where TEM means "Transverse Electric Magnetic", and m and n denote the number of times the electric field goes to zero respectively along the x- and the y-axes, respectively, i.e the transverse plane. The fundamental mode of a laser beam thus is TEM_{00}.

In order to examine the wavefronts of a monochromatic beam with wavelength λ, as shown in Figure 2.1, the wave equation describing the electric field has to be taken into account [21, 22], as

$$\nabla^2 \mathbf{E} - \frac{n^2}{c^2}\frac{\partial^2 \mathbf{E}}{\partial t^2} = 0, \tag{2.1}$$
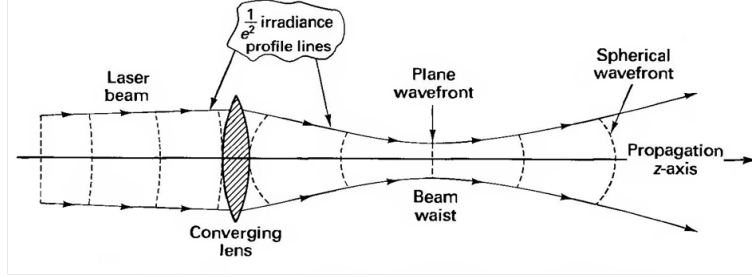
7

Figure 2.1: Schematic representation of a laser beam, the figure originates from reference [21].

Thus, it is possible to express the electric field which propagates along the z-axis with wavevector $\mathbf{k} = k\hat{z}$ as

$$\mathbf{E} = \mathbf{U}(x, y, z) \, e^{i(kz - \omega t)}. \tag{2.2}$$

The $\mathbf{U}(x, y, z)$ function provides the details of the wave intensity and phase in the x-, y-direction, i.e., the transverse plane. Solving Equation 2.1 in the paraxial approximation, there is a cylindrical symmetry in the laser beam's electric field magnitude in the propagation direction. Hence, defining $\rho^2 = x^2 + y^2$ yields to

$$\mathbf{U}(\rho, z) = \mathbf{E}_0 e^{i\left[P(z) + \frac{k\rho^2}{2q(z)}\right]}. \tag{2.3}$$

In this relation $P(z)$ and $q(z)$ are complex parameters of the beam representing a phase shift along the propagation axis and the complex radius of curvature, respectively. In order to characterize the beam, it is possible to express the complex radius of curvature as function of two real parameters:

$$\frac{1}{q(z)} = \frac{1}{R} + i \frac{\lambda}{\pi w^2}, \tag{2.4}$$

where $R(z)$ is the radius of curvature of the wavefront and $w(z)$ is the transverse dimension of the beam. The beam width is defined as the distance from the axis when the intensity drops to $1/e^2$. Both R and w are parameters with physical meanings, thus they can be measured in order to characterize the beam. Comparing Equation 2.3 with 2.4, it is possible to express the behaviour of both the radius of curvature and the beam transverse size in terms of the spot size w_0 at the beam waist, i.e., the minimum beam size, and the distance z from the beam waist. These relations read as follows

$$w(z)^2 = w_0^2 \left[1 + \left(\frac{\lambda z}{\pi w_0^2} \right)^2 \right], \tag{2.5}$$

$$R(z) = z \left[1 + \left(\frac{\pi w_0{}^2}{\lambda z} \right)^2 \right].$$
(2.6)

Defining the Rayleigh range z_R as

$$z_R = \frac{\pi w_0{}^2}{\lambda}$$
(2.7)

and replacing it into Equation 2.5 leads to another useful relation:

$$w(z_R) = w_0 \sqrt{2},$$
(2.8)

consequently the Rayleigh range is a measure of the length of the waist region (Figure 2.2).
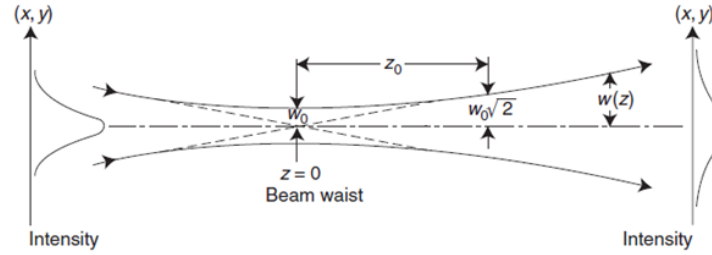

Figure 2.2: Variation of the beam size $w(z)$ of a Gaussian Beam, Ref. [22].

Through the definition of z_R it is also easy to express the beam size and the radius of curvature of the beam as

$$w(z)^2 = w_0{}^2 \left[1 + \left(\frac{z}{z_R} \right)^2 \right] \qquad\qquad R(z) = z \left[1 + \left(\frac{z_R}{z} \right)^2 \right]$$
(2.9)

Furthermore combining Equation 2.3 with 2.4 the transversal intensity distribution is proved to be Gaussian, as shown in Equation 2.10, with peak value on the $z-$axis.

$$\mathbf{U}^*\mathbf{U} \propto e^{-\frac{2r^2}{w^2}}$$
(2.10)

2.1.1 Gaussian beams propagation

A beam remains Gaussian as it propagates in vacuum, however, both the beam spot size and the radius of curvature change along the propagation as expressed in Equations 2.9. Vacuum can be thought as an optical element made up of an empty section of length z. Thus, considering the evolution in vacuum of the q parameter between two parallel planes, transverse to the propagation direction, at $z = z_i$ and $z = z_f$, it results

$$q_f = q_i + (z_f - z_i)$$
(2.11)

where $q_i = q(z_i)$ and $q_f = q(z_f)$.

The effect of optical elements, such as lenses and mirrors, on light rays is described through the use of a matrix method: the propagation of a Gaussian beam obeys to the so called "ABCD Law", a method that allows an easy estimate of the changes in q parameter and can be applied to every optical system in paraxial approximation. The evolution of the q parameter can be then described by four parameters A, B, C, D through

$$q_f = \frac{Aq_i + B}{Cq_i + D}. \tag{2.12}$$

It is thus possible to define the so called *system's ray matrix*, or *ABCD matrix*, $M = \begin{pmatrix} A & B \\ C & D \end{pmatrix}$.
This method applies to every optical system in paraxial approximation.
Taking into account a system of consecutive elements, the system ray matrix is provided by the ray matrix of the first optical element encountered, multiplied on the left by the ray matrix of the second element, and so forth, [22], that yields to

$$M_{system} = M_n \cdots M_2 \cdot M_1 \tag{2.13}$$

In this project only the ray matrices for three different simple optical elements are going to be considered:

- Propagation through a medium of length d and refractive index n $\qquad M_d = \begin{pmatrix} 1 & \frac{d}{n} \\ 0 & 1 \end{pmatrix}$

- Propagation through a thin lens of focal length f $\qquad M_f = \begin{pmatrix} 1 & 0 \\ -\frac{1}{f} & 1 \end{pmatrix}$

- Reflection due to a curved mirror with radius of curvature R, $\qquad M_R = \begin{pmatrix} 1 & 0 \\ -\frac{2}{R} & 1 \end{pmatrix}$

2.2 Optical cavity

In this section a fundamental element in optics is going to be analyzed, element that it is also a critical component for obtaining a laser: the optical cavity or optical resonator. An optical cavity consists of a system of mirrors and lenses that confines light through multiple reflections producing standing waves for certain resonance frequencies. Henceforth, the analysis of a beam light incident upon a two-mirror cavity, with no optical elements in between, is described: this particular cavity is known as *Fabry-Pérot Resonator* [23].

Consider the scheme of Figure 2.3: two mirrors of reflectivity $\mathcal{R}_1$ and $\mathcal{R}_2$ placed at a distance L_{cav}, called *cavity length*. The medium inside the cavity is characterized by the refractive index n.
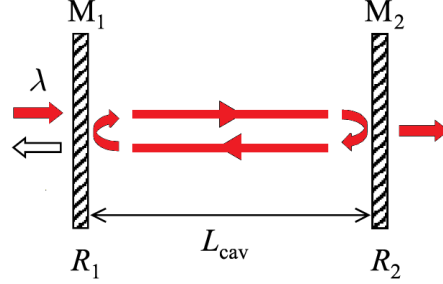

Figure 2.3: Light of wavelength λ is introduced through one of the mirrors of a Fabry-Pérot resonator of length L_{cav}, composed of two mirrors M_1 and M_2 characterized by reflectivity $\mathcal{R}_1$ and $\mathcal{R}_2$ respectively.

Introducing a beam with wavelength λ through one side of the cavity, the transmission $\mathcal{T}$ of the light through the other side, assuming that there are no absorption or scattering losses within the cavity, is given by [25]

$$\mathcal{T} = \frac{1}{1 + \frac{4\mathcal{F}^2}{\pi^2} sin^2\left(\frac{\phi}{2}\right)} \tag{2.14}$$

where

$$\phi = \frac{4\pi n L_{cav}}{\lambda} \tag{2.15}$$

represents the *round-trip phase shift*, while

$$\mathcal{F} = \frac{\pi (\mathcal{R}_1 \mathcal{R}_2)^{\frac{1}{4}}}{1 - (\mathcal{R}_1 \mathcal{R}_2)^{\frac{1}{2}}} \tag{2.16}$$

is the *finesse* of the cavity, a parameter that depends only on the mirrors' properties.
From Equations 2.14 and 2.15 it is evident that, assuming no absorption and no scattering losses, the transmission $\mathcal{T}$ equals to 1 when the round-trip phase shift is $\phi = 2\pi m$, i.e when the light bouncing around the cavity is in phase each trip around. This condition happen only if L_{cav} is equal to a m integer number of intracavity half wavelength. In this situation the cavity is said to be *on-resonance*.

Considering the longitudinal modes of the ray, the resonant modes and the free spectral range result

$$\omega_m = \frac{m\pi c}{n L_{cav}} \qquad \qquad \Delta\omega = \frac{\pi c}{n L_{cav}}. \tag{2.17}$$

Analyzing the transmission spectrum of a resonant cavity, Figure 2.4, it is evident that it is sharply peaked on the round-trip phase shift: Equations 2.14 and 2.15 imply that the full width at half maximum (FWHM) may be expressed as

$$\Delta\omega_{FWHM} = \frac{\Delta\omega}{\mathcal{F}}. \tag{2.18}$$

It is thus clear that the finesse of the cavity determines its resolving power.
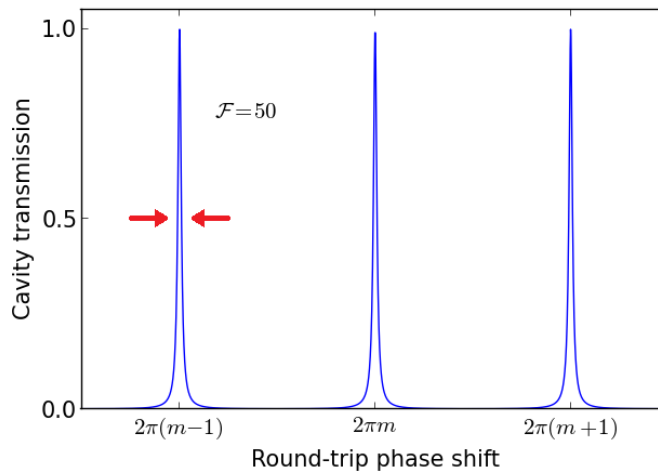

Figure 2.4: Transmission spectrum simulated for a lossless cavity with finesse $\mathcal{F} = 50$. Resonance occurs whenever the round-trip phase equals $2\pi m$, where m is an integer.

Another established parameter to characterize a cavity is the *quality factor Q* of the the cavity, given by

$$Q = \frac{\omega}{\Delta\omega_{FWHM}} = \frac{L_{cav}\,(\mathcal{R}_1\mathcal{R}_2)^{\frac{1}{4}}\,\omega}{c\left[1 - (\mathcal{R}_1\mathcal{R}_2)^{\frac{1}{2}}\right]} \tag{2.19}$$

that, like the finesse, is a measure of the sharpness of the frequency transmission, but unlike the finesse, it depends also on the cavity length and not only on the properties of the mirrors.

Another quantity that should be taken into account in the characterization of a cavity is the photon lifetime inside the cavity. Consider a light source at the center of a high finesse cavity with $\mathcal{R}_1 \approx \mathcal{R}_2 \approx \mathcal{R} \approx 1$, that emits a short pulse of light composed of N photons. After a range of time $\Delta t = 2L_{cav}/c$ the pulse should have completed a round-trip and the number of photon should be equal to $\mathcal{R}^2 N$. This process continues until all the photons are lost from the cavity. That yields to

a *photon decay rate* κ, defined as

$$\kappa = \frac{c\left[1-(\mathcal{R}_1\mathcal{R}_2)^{\frac{1}{2}}\right]}{L_{cav}\,(\mathcal{R}_1\mathcal{R}_2)^{\frac{1}{4}}} = \frac{\omega}{Q}. \tag{2.20}$$

It is evident from Equations 2.19 and 2.20 that there is a connection between the quality factor and the photon decay rate, $\kappa = \omega/Q$.

Cavity Stability

In the previous sections the analysis considered only the effects of two parallel reflecting surfaces on a plane wave incident normally on them. Therefore the consequences of having a beam that is "almost" a plane wave have to be included: it is verified that mirrors with a certain specific curvatures exhibit lower diffraction losses for each round-trip reflection [23]. Moreover the alignment tolerance of the cavity for curved mirror are definitely less stringent than those for plane-parallel mirrors. In order to have a stable cavity the propagating ray should have the same q parameters on the mirrors after a round-trip, otherwise the beam would diverge and exit the cavity after a large number of passes back and forth within the cavity itself.

It is possible to derive the stability criteria of the cavity using the ABCD method [24].

$$-1 < \frac{A+D}{2} < 1 \tag{2.21}$$

In literature there is another equivalent way to express the stability criteria of the cavity [23], that is

$$0 < g_1 g_2 < 1 \tag{2.22}$$

where $g_i = 1 - \frac{L_{cav}}{R_i}$ and R_i represents the radius of curvature of the ith mirror. These conditions may also be represented in a graph, as in Figure 2.5.
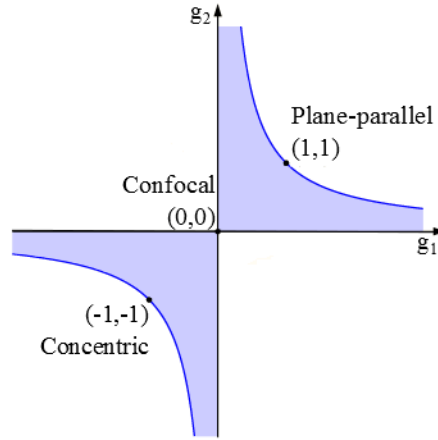
Figure 2.5: Stability diagram for a two-mirror cavity.

In a stable resonator, the fundamental Gaussian mode waist spot size w_0, expressed in terms of the Rayleigh range z_R and of the stability parameters g_1 and g_2, is given by [23]

$$w_0^2 = \frac{\lambda z_R}{\pi} = \frac{L_{cav}\lambda}{\pi} \sqrt{\frac{g_1 g_2 (1 - g_1 g_2)}{(g_1 + g_2 - 2g_1 g_2)^2}}, \tag{2.23}$$

while the mirror locations relative to beam waist are

$$z_{1,2} = L_{cav} \frac{g_{2,1} (1 - g_{1,2})}{g_1 + g_2 - 2g_1 g_2}. \tag{2.24}$$

The beam sizes at the mirrors are given by

$$w_{1,2}^2 = \frac{L_{cav}\lambda}{\pi} \sqrt{\frac{g_{2,1}}{g_{1,2} (1 - g_1 g_2)^2}}. \tag{2.25}$$

These variables are very important in the perspective of coupling the output of the cavity to an optical fiber, which is the aim of the project. In the case of an half symmetric cavity, which is a cavity with a flat mirror ($R_1 = \infty$) and a curved one (R_2), i.e., the cavity that is going to be investigated in this project, the beam size on the curved mirror results

$$w_2^2 = \frac{L_{cav}\lambda}{\pi} \sqrt{\frac{1}{g_2 (1 - g_2)^2}}. \tag{2.26}$$

The mode volume within the Gaussian fundamental mode is obtained through integration of the

electric field distribution as

$$V_{00} = \int_0^{L_{cav}} \frac{w_0^2}{w^2(z)} dz \int_{-\infty}^{+\infty} \int_{-\infty}^{+\infty} e^{-2x^2/w^2} e^{-2y^2/w^2} dxdy = \frac{\pi w_0^2}{2} L_{cav}. \quad (2.27)$$

Thus the mode volume depends only on the cavity length and on the size spot on the waist.

2.2.1 Loss mechanisms

In the previous sections an ideal lossless cavity was described. However in real cavities there are many loss mechanisms, such as cavity leakage, or clipping losses. Moreover taking into account fiber based resonators, another important loss mechanism arises from the coupling efficiency between the cavity and the output fiber. These mechanisms are going to be analyzed one by one hereafter.

Cavity leakage
The losses inside the cavity are another quantity that characterizes a cavity.
Consider a cavity composed of two mirrors, labelled i=1,2, the round-trip loss $\mathcal{L}_{tot}$ is given by [19]

$$\mathcal{L}_{tot} = \mathcal{T}_1 + \mathcal{T}_2 + \mathcal{L}_1 + \mathcal{L}_2 \quad (2.28)$$

where $\mathcal{T}_i$ represents the transmission and $\mathcal{L}_i = \mathcal{S}_i + \mathcal{A}_i$ the scattering and absorption losses of the ith mirror.
In presence of losses the cavity finesse results

$$\mathcal{F} = \frac{\Delta\omega}{2\kappa} = \frac{2\pi}{\mathcal{L}_{tot}}. \quad (2.29)$$

Therefore is fundamental to estimate the scattering losses for a cavity characterization. The scattering losses are due to the roughness of the mirrors' surface. More specifically there is a relation between the total integrated scattering $\mathcal{S}$ from a surface for a light incident normally on it and the root mean square roughness of the surface itself σ_{sc} [27], as reported in Equation 2.30.

$$\mathcal{S} = \left(\frac{4\pi\sigma_{sc}}{\lambda} \right)^2. \quad (2.30)$$

This relation enables the prediction of the scattering losses by surface profiling of the mirrors when the direct measurements are difficult to realize.

Clipping Losses

Using fiber based resonators, the small effective diameter of the mirror's structure introduces an-other leakage mechanism: light is scattered out of the cavity when the wavefront curvature and the mirror curvature are too different or when it hits the convex part of the mirror structure [28].

The clipping losses depend on the mirror. From Equation 2.29 it is evident that if the clipping losses are expected to contribute to the total one less than 10% $\mathcal{L}_{cl} < \frac{\pi}{5\mathcal{F}}$, that yields to

$$a > w\sqrt{\frac{ln\left(\frac{5\mathcal{F}}{\pi}\right)}{2}}. \tag{2.31}$$

The clipping losses on the mirror add to the scattering and absorption losses, thus the losses on the ith mirror are given by

$$\mathcal{L}_i = \mathcal{S}_i + \mathcal{A}_i + \mathcal{L}_{cl}. \tag{2.32}$$

Fiber coupling efficiency

In the optical cavity of interest the output should be collected by a single-mode (SM) optical fiber. The efficiency of coupling from the cavity into the single-mode fiber has thus a crucial role. The experimental estimation of the above-mentioned quantity is hard to carry out, however it can be analytically calculated as in Ref. [29].
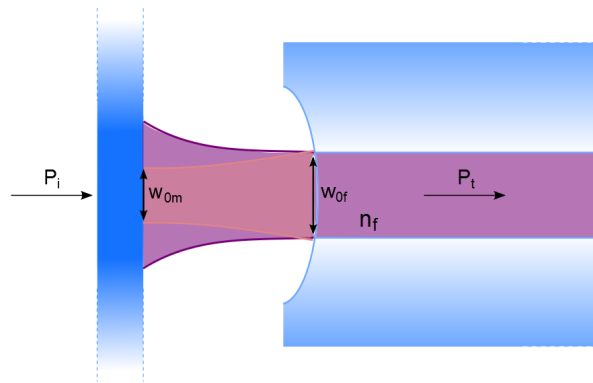

Figure 2.6: Schematic representation of the mode matching between the cavity mode w_m (pink mode) and a SM fiber transverse mode w_f (purple mode). The cavity consists in a planar mirror and a concave mirror obtained on a SM fiber end facet.

Consider the coupling efficiency between the light in a SM fiber incident onto the mirror

of a FFPC and the cavity mode, assuming both modes to be Gaussian, as in Figure 2.6. The lensing effect of the concave fiber mirror and the mismatch of the wavefront curvatures are taken into account, while any offset or tilting misalignment between the mirror and the fiber axis are neglected. The coupling efficiency for a fiber transverse mode with size w_f and a cavity mode with spot size w_m results

$$\varepsilon = \frac{4}{\left(\frac{w_f}{w_m} + \frac{w_m}{w_f}\right)^2 + \left(\frac{\pi n_f w_f w_m}{\lambda R}\right)^2}.$$ (2.33)

where n_f is the refractive index of the fiber and R the radius of curvature of the fiber's concave structure.

Neglecting the lensing effect of the concave structure and the mismatch of the wavefront curvatures amounts to assume

$$\left(\frac{\pi n_f w_f w_m}{\lambda R}\right)^2 \ll \left(\frac{w_f}{w_m} + \frac{w_m}{w_f}\right)^2,$$ (2.34)

that is a good approximation in many cases [19] and yields to a simple estimate of the coupling efficiency as

$$\varepsilon = \left(\frac{2w_f w_m}{w_f^2 + w_m^2}\right)^2.$$ (2.35)

In the case where a multi-mode (MM) fiber accounts for the outcoupling side, the coupling coefficient is determined by its *numerical aperture N.A.* $= sin(\theta_{acc})$. The angle θ_{acc} represents the acceptance angle of the fiber, which should be bigger than the divergence angle of the cavity mode to avoid the damping. The divergence angle can be defined as $\lambda/(\pi w_0)$, thus the condition to avoid damping with a MM fiber equals to

$$w_0 > \frac{\lambda}{\pi \, arcsin(N.A.)}.$$ (2.36)

2.2.2 Atom-cavity coupling

Assume that there is an atom inserted in a cavity, so that it absorbs photons from the cavity mode and also emits into the cavity through radiative emission. If the frequency of the atom's electromagnetic emission coincides with the one of the resonant modes of the cavity, this enhances the interaction between the atom and the light field since atom and cavity can exchange photons in a resonant way [25]. The transition frequencies of an atom are determined by its own internal structure, therefore in this analysis it is considered fixed. The resonant condition is then achieved by tuning the cavity to have one of the cavity modes' frequency coinciding with the atom transition.

The relative strength of the atom-cavity interaction is determined by three different parameters:

- the photon decay rate of the cavity (κ);

- the non-resonant decay rate (γ);

- the atom-photon coupling parameter (g_0).

The photon decay rate, depending only on the cavity, has already been defined by the Equation 2.20.

The non-resonant decay rate instead takes into account different contributions. The atom could decay to other levels emitting a photon with a frequency that does not coincide with the resonant ones, else it could emit a photon of the resonant frequency, but in a direction that does not coincide with the cavity mode. The first process is connected to the internal structure of the atom, while the second one concerns the cavity. The combination of the effects causes dephasing. In the case of radiative decay to non-resonant photon modes the decay rate equals to

$$\gamma = \frac{A_{12}\,(4\pi - \Delta\Omega)}{8\pi} \tag{2.37}$$

where A_{12} represents the Einstein coefficient for spontaneous emission into free space [26], and $\Delta\Omega$ the solid angle subtended by the cavity mode.

The atom-photon coupling parameter is connected to the interaction between the atom and the vacuum field that exists in the cavity due to the zero-point fluctuations of the electromagnetic field.

These three parameters define the characteristic time-scale for the dynamics of the atom-photon system, leading to two different coupling regimes.

If $g_0 \ll (\kappa, \gamma)$, the emission rate is influenced by the cavity, but the photons, as in free space spontaneous emission, cannot be re-absorbed: the system is in the **weak coupling** limit.

The weak coupling limit thus occurs when the atom-cavity coupling constant is smaller than the loss rate due to either leakage of photons from the cavity or decay to non-resonant modes. The loss of photons in the system is faster than any characteristic interaction between cavity and atom. The emission of light is ergo "irreversible".

If $g_0 \gg (\kappa, \gamma)$, the interaction is faster than the loss of photons out of the cavity mode, thus the photons may be re-absorbed by the atom before being lost by the cavity: the system is in the **strong coupling** limit. It is evident from the relation between κ and the quality factor (Equation 2.20), that, in order to obtain a strong coupling system, $g_0 \gg \frac{w}{Q}$ which requires high Quality factors.

In the strong coupling conditions the interaction between atom and photon in the cavity mode is reversible: the emitted photon into the resonant mode is re-absorbed by the atom faster than the loss process. This regime of interaction is called *cavity quantum electrodynamics*. The coupling of a two-level atom with a single mode cavity is described by *Jaynes-Cummings model* [25].

The electric-dipole interaction between atom and photon mixes the degenerate states and lifts the degeneracy: the mixed atom-photon states are called *dressed states*.

In either regime the effect of the cavity is either to enhance or suppress the radiative emission rate compared to free space, depending on the resonance with the cavity mode.

The enhancement of the emission rate on resonance in a cavity is due to the so called **Purcell effect**. Consider a two-level atom in a single-mode cavity of mode volume V_0. "Single-mode cavity" means that there is only one resonant mode of the cavity that is close to the emission frequency of the atom. A convenient parameter that characterizes the effect of the cavity, is the *Purcell factor F_P*, also called cooperativity parameter [30], that is defined as the ratio between the probability of emission in the cavity W^{cav} and the probability of emission in free space W^{free}:

$$F_P = \frac{W^{cav}}{W^{free}}. \tag{2.38}$$

At the exact resonance, in the dipole approximation and with the dipoles orientated along the field direction, the Purcell factor reduces to [25]

$$F_P = \frac{3Q\lambda^3}{4\pi^2 V_0}. \tag{2.39}$$

Equation 2.39 shows that large Purcell factors requires cavity with high quality factors and small modal volumes. The enhancement of the emission rate on resonance is related to the large density-of-states function at the cavity mode frequency, while the inhibition of the off-resonance emission is due to the absence of photon modes into which the atom can emit. A useful way to express the Purcell factor of a single atom in a FFPC, i.e., a typical single-photon source, is [19]

$$F_P = \frac{6\lambda^2}{\pi^3} \frac{\mathcal{F}}{w_0^2}. \tag{2.40}$$

where w_0 represent the cavity mode waist.

2.3 Nitrogen-vacancy centers in diamond

Nitrogen-vacancy (NV) centers are one of the many well studied luminescent defects in diamond [31]. They consist in a substitutional nitrogen atom in the diamond structure, with a vacancy trapped at an adjacent lattice position (as shown in Figure 2.7), oriented in the [111] crystalline direction [33].

These color centers are commonly prepared in type I_b synthetic diamonds, that contain single substitutional nitrogen impurities homogeneously dispersed. These diamonds are irradiated with

electrons, protons or neutrons in order to induce additional vacancies, that are allowed to diffuse next to the nitrogen by annealing processes at $900°C$.
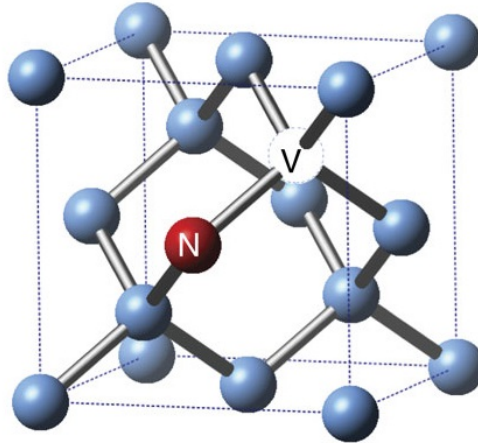

Figure 2.7: FCC lattice structure of diamond with an NV color center, Ref. [32].

The NV centers exist in two different charged states: NV^0, the neutral charge state, and NV^-, the negatively charged state, where an electron is trapped in the vacant site. As both centers states are characterized by large optical absorption cross-sections, short excited state lifetimes and high quantum yields, they can be used as efficient single-photon sources [33, 34]. Furthermore, both of them have been proved to be extremely photostable under off-resonance excitation (532 nm), without evidence of photobleanching [13].
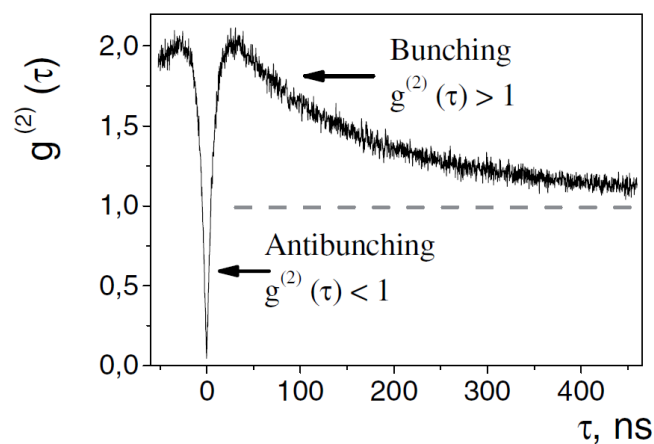

Figure 2.8: Second-order correlation function of the fluorescence intensity of a NV center at room temperature [35].

In order to demonstrate the quantum properties of the fluorescence emitted by an NV center, the *second order correlation function* $g^2(\tau)$ (Appendix A) can be measured verifying that NV centers are single-photon source (Figure 2.8), as in [34].

This project is going to focus on NV^- centers, thus from now on NV centers refers implicitly to the negatively charged state.

The fluorescence spectrum of an NV center (Figure 2.9) presents a broad emission bandwidth spanning over 100 nm. In particular after pumping the NV center to an excited states, e.g. with a 532 nm laser source, it may decay to the ground state through radiative emission. It is possible to identify the zero phonon line (ZPL), i.e., the wavelength at which the relaxation is not phonon assisted, at $\lambda = 637.2$ nm corresponding to $E = 1.945$ eV and the phonon-side band (PSB). The radiative decay time of the ZPL has been measured to be 13 ± 0.5 ns [36].
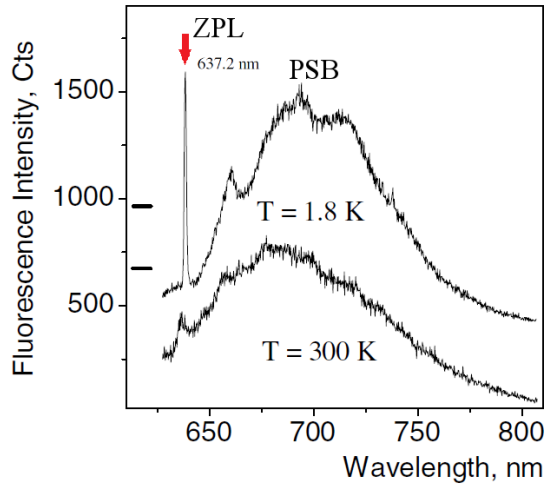

Figure 2.9: Fluorescence emission spectra of single NV^- centers at room temperature and LHe temperature. The ZPL(red arrows) is at $\lambda = 637.2$ nm corresponding to $E = 1.945$ eV [35]

2.4 Laser micro-fabrication in silica

Lasers provide the ability to deliver high amounts of energy into confined regions of a material. Additionally laser processing gives the advantage of a precise control of the amount of deposited energy on the region of its injection. In particular CO_2 laser light is a powerful tool for surface processing of fused silica by thermal effects. Silica indeed present a strong absorption of the 10.6 μm wavelength, i.e., the typical CO_2 laser light wavelength. The heat thus is absorbed within few microns of material, that enables a controlled surface melting. This powerful tool has been

Density	ρ	$2.2 \cdot 10^3$ kg/m^3
Specific heat	C	750 J kg^{-1} K^{-1}
Thermal diffusion constant	D	$8 \cdot 10^{-7}$ m^2 s^{-1}
Material removal rate constant	v_0	$3.8 \cdot 10^3$ m s^{-1} [37]
Latent heat per atom	U	3.6 eV [38]

Table 2.1: Material properties of fused silica

used for different applications, such as polishing optical surfaces, tapering optical fibers, damage repair of optical elements, formation of microspherical and microtoroidal resonators and surface texturing.

This project will focus on how thermal heating induced by CO_2 laser light imprints smooth concave structures on silica, in order to obtain concave fiber tips to use in a fiber Fabry-Pérot resonator. The process used relies on single laser pulse train with high intensity, in a regime where surface evaporation is the dominant process: material removal by evaporation leads to shape a depression, while the melting is restricted to a thin layer that only smoothens the surface on the nanometers scale.

In order to understand the physical process leading to the formation of these ultra-smooth concave structures, consider a CO_2 laser beam imping onto fused silica. The beam is partially reflected and partially absorbed within a layer of few microns, because of the absorption band of silica around 9-9.5 μm, due to the anti-symmetrical stretching mode of Si-O-Si [39]. Material properties of fused silica are illustrated in Table 2.1.

In order to have an analytical determination of the heat distribution $Q(r,z)$ transmitted by the power source, it is convenient to introduce the complex refractive index $m_\lambda = n_\lambda + ik_\lambda$ of silica glass at wavelength λ. In particular n_λ represents the *refractive index* and k_λ the *absorption index*. Through this parameters the *Fresnel reflection coefficient R* is defined as [39]

$$R = \frac{1 - n_\lambda - ik_\lambda}{1 + n_\lambda + ik_\lambda}. \tag{2.41}$$

By means of Equation 2.41 it is possible to obtain an expression of the heat source profile in case of Gaussian laser beam of waist size w_0 [28, 38]

$$Q(\mathbf{r},z) = \frac{2P(1-R)\alpha_\lambda}{\pi w_0^2} e^{-\alpha_\lambda z} e^{-2\frac{r^2}{w_0^2}}, \tag{2.42}$$

where P represents the laser power reaching the silica surface and α_λ is the *absorption coefficient*, connected to the imaginary part of the complex refractive index through the relation $\alpha_\lambda = 4\pi k_\lambda/\lambda$. This expression for the heat source can be used to study the evolution of the temperature profile

$T(r,t)$, described by the heat conduction equation:

$$\rho C \frac{\partial T(\mathbf{r},t)}{\partial t} - \nabla \left(\kappa \nabla T(\mathbf{r},t) \right) = Q(\mathbf{r},z) \tag{2.43}$$

where ρ represents the density, t is the time, C is the *specific heat*, κ is the *thermal conductivity*. An analytic solution of Equation 2.43 is found considering as heat source laser pulses of Gaussian form with temporal pulse-shapes assumed to be rectangular, with pulse-length τ. This solution is given by the expression [20, 40]

$$T(r,\tau) = \frac{P(1-R)}{w_0^{\frac{3}{2}}\sqrt{\pi}} \frac{\sqrt{D}}{\kappa} \int_0^\tau \frac{e^{-\frac{r^2}{w_0^2/2+4D\tau'}}}{\sqrt{\tau'}\left(\frac{w_0^2}{2}+4D\tau'\right)} d\tau', \tag{2.44}$$

where D represents the *thermal diffusion constant* and $P(t) = \pi w_0^2 I(t)$ is the beam power associated with the $I(t)$ intensity of the beam. The temperature in the center of the beam can be evaluated analytically from the integral and expressed in the form

$$T(0,t) = \frac{P(1-R)}{\sqrt{2\pi^3}w_0\kappa} arctan\left(\sqrt{\frac{8Dt}{w_0^2}}\right). \tag{2.45}$$

The material removal rate $v(r,t)$, i.e., the velocity of the evaporation front, is related to the local temperature as

$$v(r,t) = v_0 e^{-\frac{U}{k_B T(r,t)}}. \tag{2.46}$$

where $U = 3.6\ eV$ is the latent heat of evaporation per atom for fused silica and $v_0 = 3.8 \times 10^5$ cm/s [37]. The profile at the end of the pulse can be calculated by numerical integration of Equation 2.46.

This model however has some limitations.

- It neglects all the non-linearities, such as the strong dependence on the temperature of the thermal conductivity κ and of the absorption index k_λ of silica.

- It does not take into account the material flow caused by surface tension. This process is connected to the viscosity of fused silica that is strongly dependent on the temperature. Nevertheless low values of viscosity should be favored to avoid the contraction to convex shapes and enable smoothing over large scales [28].

- The recoil momentum caused by rapid evaporation generates pressure, that can lead to transverse flow of the melted material [37]. This recoil pressure is not considered in the model.

- Another important issue that is not taken into account is the finite size of the fiber: the

restriction of the transferred heat flow provokes heat accumulation increasing the melt and evaporation area [20].

In conclusion as already discussed in literature [28], the high number of approximations together with the properties of the fiber makes challenging the numerical prediction of the final shape of the fiber's processed surface. Consequently in this project an empirical approach to the problem is going to be carried out. In Ref. [20] however a reasonable agreement was found between the numerical implementation of this model and the observed profile diameters for silica plate machining. Thus even if there is no aim for the complete analytical solution, some dependence of the concave silica plates profiles on the laser parameters, as power and pulse-length, are going to be enhanced as we are going to see in Chapter 3.

Chapter 3

Laser-machining setup

In this project silica plates and fibers' end facets are processed through CO_2 beam pulse trains in order to obtain depressions with structural properties that make them suitable as resonator mirrors. The surface processing requires an optimized setup. In particular the setup is assembled aiming to fulfill some requirements: power stability, management of the beam profile, accurate positioning. Repeatable micro-machining results demand low power fluctuation in two different timescales: the ablation pulses scale ($\approx ms$) and the target's positioning scale ($\approx min$). Control over the adjustment in the $z-$direction, parallel to the beam, and over the beam profile avoids ellipticity effects in the imprinted structures and defines their shape (see Chapter 4). A good centering of the evaporated depression profile with the fiber's core needs accurate adjustment of the (x,y)-position of the target compared to the beam.

In Section 3.1 the general setup is outlined. Beam profiling and simulations performed to assemble the setup are exposed in Section 3.2. A presentation of a shutter obtained from an Hard Disk Drive is laid out in Section 3.3, paying close attention to its characterization. Finally the principles of the LabView driving routine of the setup are discussed in Section 3.4

3.1 Experimental setup

The laser ablation setup is schematically presented in Figure 3.1. A CO_2 laser[1] emits infrared radiation with a wavelength of 10.6 μm. The laser beam passes through a telescope-like lenses setup (i.e., lenses L_1 and L_2 in Figure 3.1) and is focused down through a 50 mm focal length lens (i.e., lens L_3 in Figure 3.1) into the target.
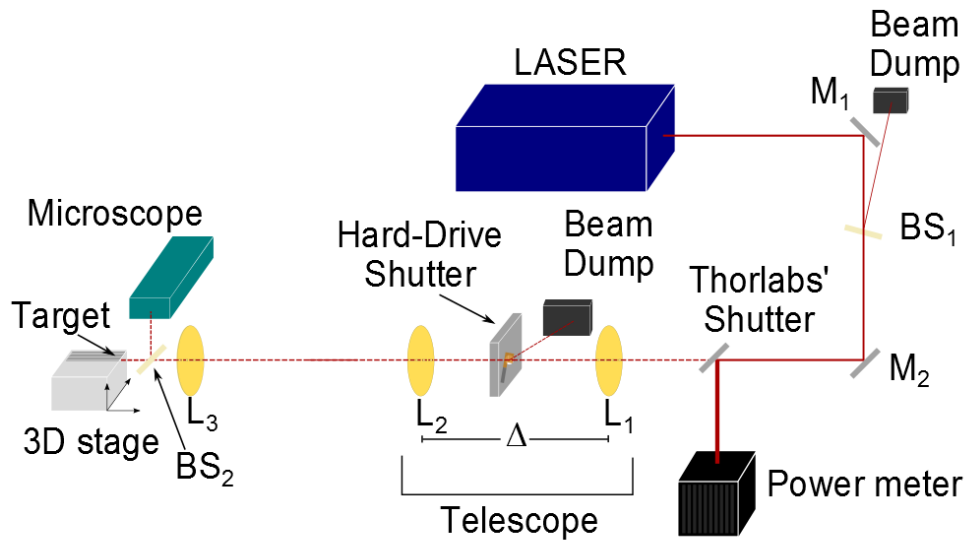
---

[1]Firestar V-series, Synrad made

Figure 3.1: Schematic representation of the setup used for silica processing. In the path mirrors are identified as *M*, beam splitters as *BS* and lenses as *L*. Δ represents the distance between L_1 and L_2.

The target consists of silica plates[2] and optical fibers, clipped mechanically or through a magnetic band respectively, on a 3d translator stage driven by differential micrometers[3]. The plates machining is the first phase of the process, in which the laser parameters are optimized according to the required properties of the concave structures (see Chapter 4). The silica plates are squared slice of fused quartz with a nominal depth of 180 μm and a typical roughness better than 2 nm. Target plates are substitute by fibers only at a later stage.

The optical fibers are magnetically clipped on grooves on the translator stage surface, in order to have the fiber cleaved end facet perpendicular to the laser beam. In this project two kind of optical fibers are used: one kind is of single mode fibers[4], the other is multimode[5]. This SM fiber type present a cladding diameter of 125 μm, a core diameter of 3.5 μm and an expected mode field diameter of $4.0 \pm 0.5 \mu$m at 630 nm. The MM fibers are characterized by a numerical aperture of N.A.=0.39, a cladding diameter of 225 μm and a core diameter 200 μm. Each fiber is stripped of its protective polymer coating and cleaved through a mechanical cleaver before the laser processing.

---

[2]SPI Supplies 01015T-AB
[3]Thorlabs MBT616D/M
[4]Thorlabs 630HP
[5]Thorlabs FT200UMT

A window[6] (i.e., BS_2 in Figure 3.1) allows the observation of the target through an optical microscope[7] connected to a charge-coupled device (CCD) camera[8]. This window presents an antireflective coating that provides less than 1% average reflectance for the $8-12$ μm spectral range, while presents high reflectance in the visible spectrum. High reflectance in the visible spectrum is required to observe the target.

The microscope and the CCD not only have the purpose of roughly investigate the target surface, but they are mainly used in the alignment of the fiber tips with the beam waist, which is critical to obtain a good coupling between the fiber mode and the cavity, as seen in Section 2.2.1. The alignment is obtained as follows: the CCD image is centered on the center of the concave structure imprinted with the CO_2 laser on the silica plates, therefore the position is hold still and the fibers are moved into focus through the translator stage relatively to this reference.

Another important element is the beam splitter (i.e., BS_1 in Figure 3.1) that is inserted in the path in order to improve the power stability of the setup. The Firestar laser has proved to have a better power stability working at higher powers, thus the use of a 85% reflector allows to run the laser at high power reducing the power fluctuations, bypassing most of the beam intensity into a beam dump.

A further method to reduce the power fluctuations is connected to the presence of the shutters. The laser presents a heat-up phase with frequent power jumps that have to be absolutely avoided for the silica processing. The laser-beam is hence bypassed through a mirror mounted on a motorized flipping holder (i.e., referred as *Thorlabs' Shutter* in Figure 3.1) into a thermal power sensor[9]. The presence of this shutter has a further advantage: the beam power is constantly monitored through the thermal power sensor. The constant knowledge of the power allows to choose the most convenient moment to laser-machine the target.

This shutter is slow compared to the machining pulse: the flipping movement requires around 0.5 s to be completed, while each depression in this project is imprinted with pulses trains of the laser beam with duration τ in the range between 5 and 500 ms. This is the reason why another faster shutter (i.e., referred as *Hard Drive Shutter* in Figure 3.1) is inserted in the beam line in the focus of the telescope-like lenses setup. Further informations about this shutter are going to be presented in Sections 3.3.

In high power CO_2 laser systems, zinc selenide (ZnSe) lenses and silver coated mirrors are required. Zinc selenide indeed has the lowest absorption coefficient of the common CO_2 transmitting materials and is, therefore, the material of choice for high-power applications at 10.6μm [41].

---

[6]Thorlabs WG71050-F
[7]Navitar 12X Zoom with 10X objective
[8]Imaging Source DMK 41BU02.H
[9]Thorlabs S310C

3.1.1 CO2 laser

The laser used in the setup is a CO_2 air-cooled pulsed laser[10]. An additional laser diode that emits at 650 nm is co-aligned with the CO_2 laser beam. This pointer serves as an accurate and convenient alignment tool and is used to test the Hard Drive Shutter, as presented in Section 3.3.

The laser is designed to operate in pulsed mode, driven by a pumping signal with frequencies up to 25kHz. The output power of the laser is controlled by adjusting the duty cycle[11] of the pulse-width modulation (PWM). For the surface treatments made in this project, the laser operates with a frequency of 20 kHz and duty cycle between 8% and 20%. The surface is then imprinted with "pulse train" of length τ generated by gating the pulsing signal through computer control, as shown in Figure 3.2.
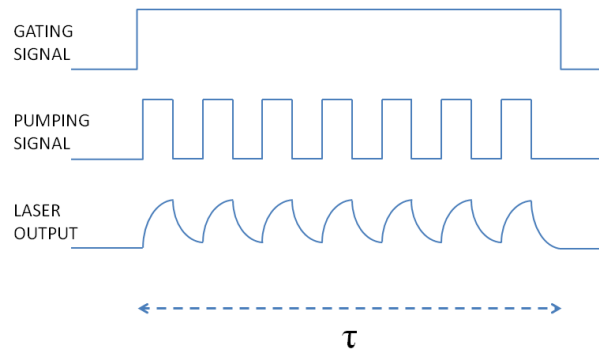

Figure 3.2: Schematic representation of the generation of a laser "pulse train" of length τ and duty cycle 50%.

In spite of the specs presented by Synrad, where the laser is guaranteed to have power stability of $\pm 3\%$ after 2 minutes [42], the laser, even after being powered on for hours, presents power fluctuations up to 10% on the minutes scale. An example of the long term beam power fluctuation is provided by Figure 3.3. The heating model presented in Section 2.4 applies for incident power of 0.3 W to 2 W [28], however the device presents a better stability for higher power, that explains the presence of the beamsplitter BS_1. Moreover the power fluctuations are the reason beyond the implementation of the shutters setup and the presence of a thermal power sensor to control the power that is truly imprinting on the surface during the machining pulse.

---

[10]Firestar V-series, Synrad made

[11]Duty cycle is defined as the percentage of one period in which a signal is active.
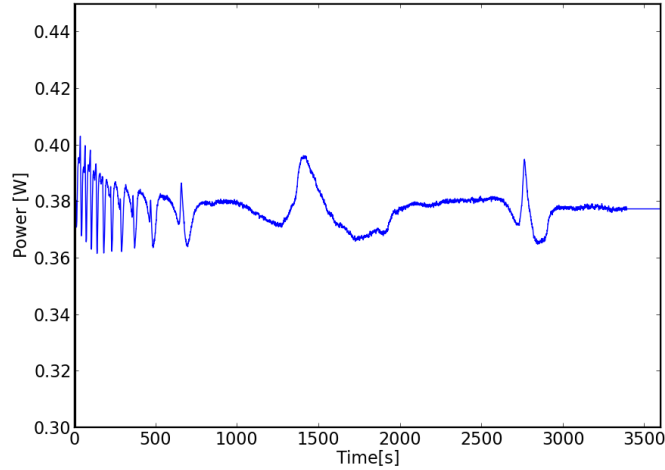
Figure 3.3: Recording of the beam power lasing for $\tau = 60$ min at duty-cycle=6%. The power is reduced by the 85% reflector BS_1.

The beam presents a slightly elliptical shape, consequently the beam width in the *x*- and *y*-directions are different. The optical path has been calibrated to minimize the difference in the widths at the target position.

3.1.2 Telescope

The telescope-like setup implemented in the path, i.e., lenses L_1 and L_2 with the shutter in between (Figure 3.1), has two main purposes. First of all the presence of a focus at the shutter location grants the fastest optical switching. Secondly the relative positions of the telescope lenses together with the final focusing lens L_3 are used to adjust the waist size at the target position.
The two telescope lenses are mounted onto a rail, in order to shift their relative position without loosing the general alignment.

The choice of the two lenses is optimized through simulations of the beam profile implemented via python routines using the matrix method. The lenses taken into account in the simulations are in a set of lenses with very various focal lengths: $-200, -100, -75, -50, -25.4, 25.4, 50, 75,$ $100, 200, 500, 750,$ and 1000 mm. Through the use of three different lenses there are many combinations that provide small waist in the telescope and that strongly focus the beam in the target, however some constrains have to be taken into account.
First of all to avoid effects as spherical aberration, a constrain should be imposed on the beam sizes at the lenses' positions. All the lenses have a diameter of 2.54 cm, so that the size of the beam on the lenses is bonded to be smaller than 6 mm [43].

Another critical aspect is that the size of the beam at the target should be tunable changing the quantity defined as Δ, i.e., the distance between the lenses in the telescope.

Finally due to the ellipticity of the beam the arrangement of the lenses should provide similar sizes of the horizontal and vertical widths of the beam in the target.

The final arrangement of the lenses recorded with their focal length is presented in Table 3.1.

f_{L_1}	d(Laser-L_1)	f_{L_2}	Δ	f_{L_3}	d(Laser-L_3)
75.0 mm	515 mm	100.0 mm	176 mm	50.0 mm	1136 mm

Table 3.1: Final arrangement of lenses in the optical path. Each lens is recorded with its focal length.

3.2   Beam profiling and simulations

Firstly, the beam width has been measured in absence of the telescope in order to estimate the beam parameters z_0 and q_0 at the laser position. Thus, simulations of the beam widths with different combination of lenses have been carried out. Finally beam size has been measured with the lenses set expressed in the previous section (Table 3.1) and compared to the simulated one.

3.2.1   Beam profiling methods

In order to characterize the beam profile, the beam width is measured along the propagation axis. This measurement has been performed through the *Knife-Edge Method*. The method consists in slicing a laser beam with a knife edge and measuring the power of the clipped beam as a function of the razor position, as reported in Figure 3.4.

The total power of the Gaussian beam is

$$P_{TOT} = I_0 \int_{-\infty}^{+\infty} e^{-\frac{2x^2}{w_x^2}} dx \int_{-\infty}^{+\infty} e^{-\frac{2y^2}{w_y^2}} dy. \tag{3.1}$$

Considering the knife edge being translated in the x-direction, the transmitted power may be expressed as

$$P(X) = P_{TOT} - I_0 \int_{-\infty}^{X} e^{-\frac{2x^2}{w_x^2}} dx \int_{-\infty}^{+\infty} e^{-\frac{2y^2}{w_y^2}} dy = \frac{P_{tot}}{2} - \sqrt{\frac{\pi}{2}} I_0 w_y \int_{0}^{X} e^{-\frac{2x^2}{w_x^2}} dx \tag{3.2}$$

Using the standard definition of the error function[12], the transmitted power results:

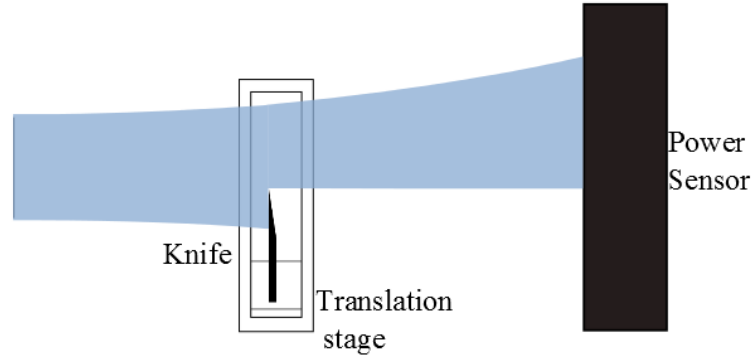$$P(X) = \frac{P_{tot}}{2}\left[1 - erf\left(\frac{\sqrt{2}X}{w_x}\right)\right]$$

(3.3)

Figure 3.4: Schematic representation of the knife-edge method to measure a beam width through a knife on a translational stage and a power sensor.

A quicker method to calculate the beam width is the *84% - 16% Method*. It requires a measurement of the total power of the beam when fully exposed and, translating the knife edge across the beam, a measurement of the distance X_{16-84} between the points at which the clipped power is 84% and 16% of the total power, positions X_{84} and X_{16} respectively.
According to Equation 3.3, at 16% power

$$0.16P_{TOT} = \frac{P_{tot}}{2}\left[1 - erf\left(\frac{\sqrt{2}X_{16}}{w_x}\right)\right] = \frac{P_{tot}}{2}erfc\left(\frac{\sqrt{2}X_{16}}{w_x}\right).$$

(3.4)

Rearranging it gives

$$erfc\left(\frac{\sqrt{2}X_{16}}{w_x}\right) = 0.32.$$

(3.5)

Therefore

$$X_{16} \approx 0.50w_x.$$

(3.6)

---

[12] The error function is defined as $erf(x) = \frac{2}{\sqrt{\pi}}\int_0^x e^{-t^2}\,dt$, while the complementary error function as $erfc(x) = 1 - erf(x) = \frac{2}{\sqrt{\pi}}\int_x^{+\infty} e^{-t^2}\,dt$.

Given the symmetry of the Gaussian function it is straightforward to see that

$$X_{16-84} = 2 \cdot X_{16} \approx 2 \cdot 0.50 w_x \approx w_x. \tag{3.7}$$

The beam profiling in this project has been obtained fitting a full set of knife edge measurements with the function of Equation 3.3. The beam waist required for the target position instead has been estimated through the 84% - 16% Method.

3.2.2 Measurement of the beam width

The beam has been measured in absence of the telescope lenses through the method described in the previous section. At different $z-$positions the beam size has been measured in both $x-$(referred to as "Horizontal") and $y-$direction (referred to as "Vertical") in order to characterize its ellipticity. Each width's estimation is reached fitting, through a python routine, the powers measured in coincidence with the motorized movement of the razor[13]. Considering the high power instability, each estimation is given by the average between the value obtained inserting the razor in the beam and the one calculated pulling it out. An example of this acquisition's method is presented in Figure 3.5.

The acquired beam sizes along the $z-$direction, Figure 3.6, are fitted through python routines using the ABCD method. The aim was to estimate the beam's parameter z_0 and q_0, respectively the position of the beam's origin relatively to the laser and the complex beam parameter associated with it. The results are shown in Table 3.2.

Direction	z_0	q_0
Horizontal	-309 ± 72 mm	-193 ± 25 mm
Vertical	-38 ± 59 mm	-279 ± 40 mm

Table 3.2: Beam parameters estimated through measurements of the beam size in absence of lenses.

The measurements suffer from the power fluctuations and jumps during the data acquisitions. This effect is emphasized by using low power lasing during the measurements, due to the energy density and damage thresholds of the thermal power sensor [43].
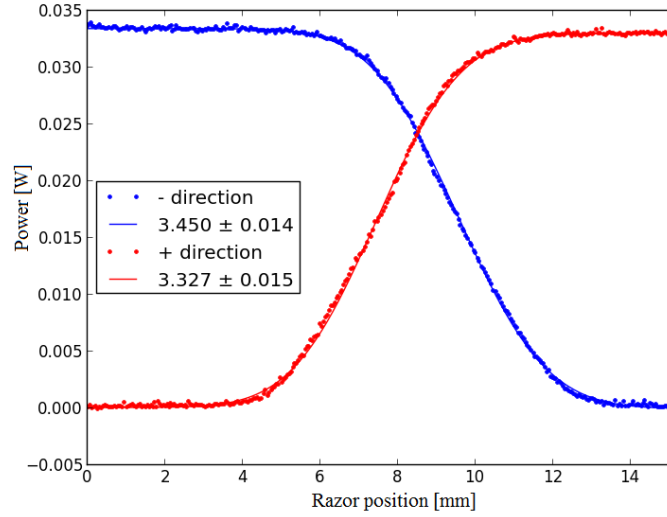
---

[13]Lego Mindstorms NXT 2.0

Figure 3.5: Plot of the beam power measured as a function of the knife edge movement on the x-direction. The "- direction" refers to the acquisition obtained inserting the razor in the beam, while "+ direction" refers to the opposite direction. The beam's sizes obtained by fitting are reported in the legend.
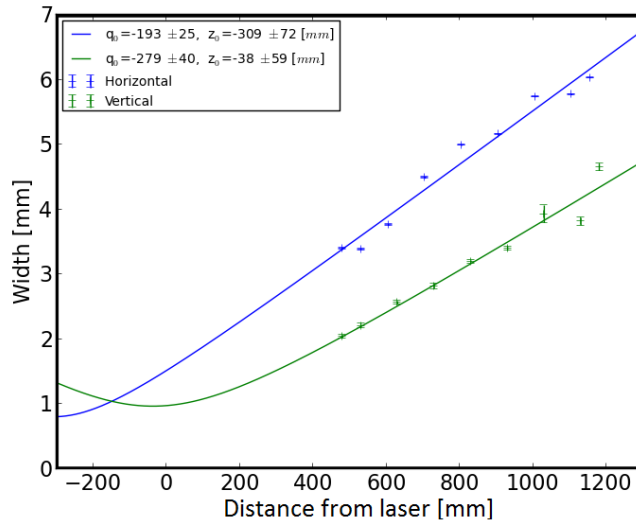

Figure 3.6: Fitting of the acquired beam sizes, measured without telescope lenses, as a function of the distance from the laser (z=0 mm). "Horizontal" refers to the beams sizes in the $x-$direction, while "Vertical" to the $y-$direction. The beam's parameters are reported in the legend. z_0 and q_0 respectively characterize the position of the beam's origin relatively to the laser and the complex beam parameter.

3.2.3 Beam simulations

As mentioned in Section 3.1.2, simulations of the beam profile with different combinations of telescope lenses are carried out, using the beam parameters expressed in Table 3.2. The lenses' choice that better applies to the required conditions is shown in Table 3.1, leading to the simulated beam profiles presented in Figure 3.7.
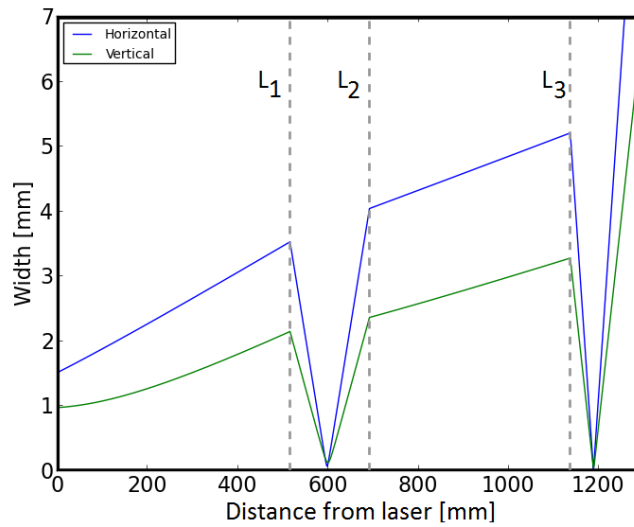

Figure 3.7: Simulated beam profile with lenses L_1, L_2 and L_3, respectively with focal lengths of $f(L_1) = 75$ mm, $f(L_2) = 100$ mm and $f(L_3) = 50$ mm. The grey dash lines point out the presence of the lenses. "Horizontal" refers to the beams sizes in the $x-$direction, while "Vertical" to the $y-$direction. The beam's parameter z_0 and q_0 used in this simulation are expressed in Table 3.2.

The profile exhibits two evident focuses. The first one, between the telescope lenses, enhanced in Figure 3.8(a), presents an horizontal waist of $w_0 = 0.078$ mm and a vertical one of $w_0 = 0.132$ mm. The simultaneous minimum size of both the vertical and horizontal direction take place in the y-direction waist, thus the vertical waist is considered the minimum beam size in the telescope for the following analysis. Similarly at the target position, Figure 3.8(b), the simulation of the horizontal waist results of $w_0 = 0.033$ mm, while the vertical one of $w_0 = 0.053$ mm.
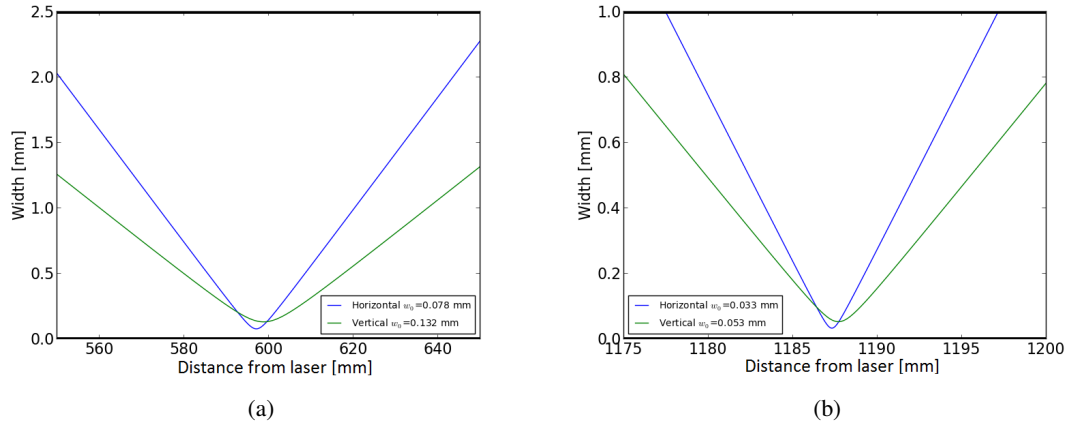
Figure 3.8: Closer view of beam profile of Figure 3.7 at the telescope waist (a) and at the target waist (b).

3.2.4 Telescope's length optimization

An further study of the beam profile consists in measuring the beam size at a 25 mm distance before lens L_3, changing the relative position of the telescope lenses. The second lens L_2 is shift onto the rail relatively to L_1, with distance Δ in the range between 173 and 220 mm. This measurements are fitted through the ABCD method for a new estimation of z_0 and q_0, as in Figure 3.9. It is worth noting that data with Δ in the range between 173 and 175 mm are not considered in the fitting: they are evidently lower than expected. Likely the beam was too wide to be fully collected by the active area of the thermal power sensor, thus the beam was partially cropped and the measurements are inaccurate.

Defining the compatibility between two measurements A and B as $\frac{|A-B|}{\sqrt{\sigma_A^2+\sigma_B^2}}$, the resulting beam parameters are highly incompatible with the one expressed in Table 3.2. The complex beam parameter in the horizontal direction results $q_0 = -71 \pm 3$ mm compared to the previous estimation of -193 ± 25 mm, with compatibility of 4.8, and $z_0 = -42 \pm 3$ mm compared to -309 ± 72 mm, with compatibility of 3.7. The beam profile is thus simulated again starting from these parameters, as reported in Figure 3.10.

The horizontal beam waist in between the telescope lenses in this additional simulation results $w_0 = 0.075$ mm, with a difference of 4% from the previous simulation. The horizontal beam waist at the target position turns out to be $w_0 = 0.029$ mm, with a difference of 12% from the previous simulation, but still of the same order.
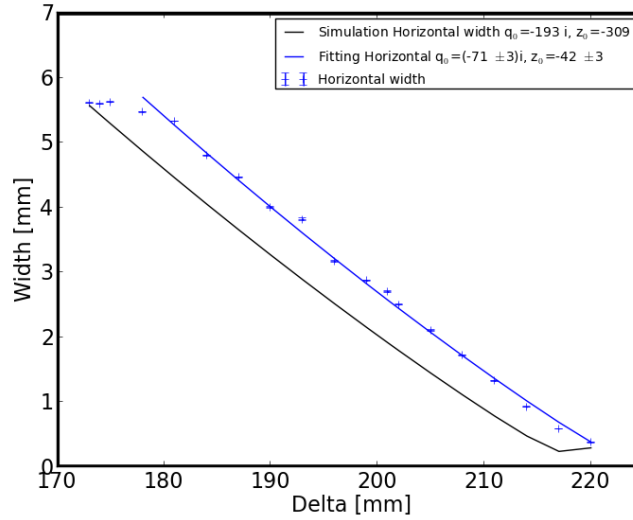
Figure 3.9: Fitting of the beam size 25 mm before L_3 traced against the distance Δ between the telescope lenses L_1 and L_2. The black bold line represents the beam size simulated through the parameters expressed in Table 3.2.

The measured beam size at the target position is of $w_x = 0.058 \pm 0.005$ mm and $w_y = 0.062 \pm$ 0.006 mm. This estimation is obtained through repeated measurements of the beam size in both directions through the *84% - 16% Method* presented in Section 3.2.1, using a razor fixed to the translational stage that holds the target. The use of the motorized razor is forbidden by the very compact structure of the set-up close to the target position. The slower manual measurement combined with the power fluctuation of the laser at low temperature makes a good estimation of the beam size challenging.
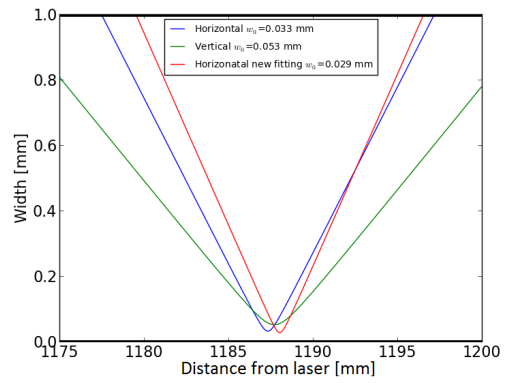
The difference between the measured beam size and the simulated one at the target position may be explained by the presence of the window, i.e., BS_2, a thick optical device that is neglected in the simulations.
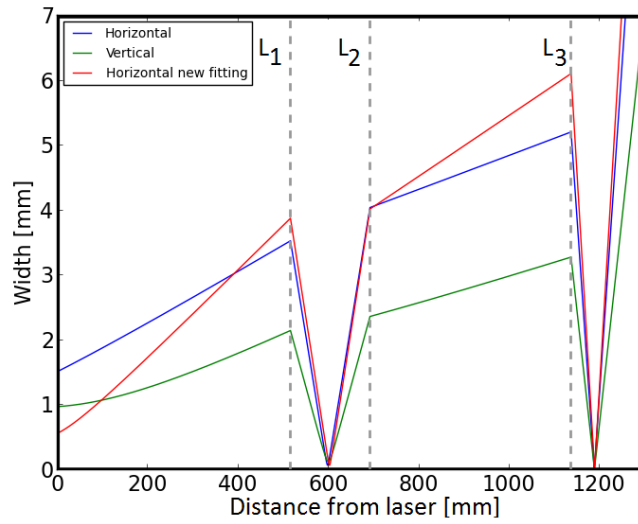
(a)
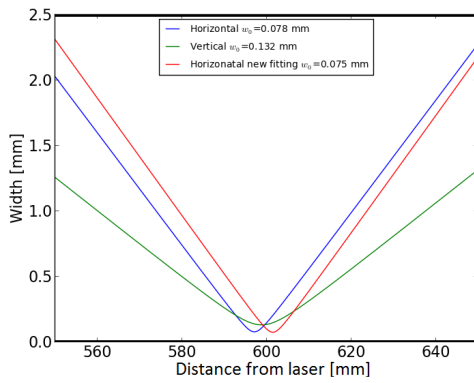
(b)

(c)

Figure 3.10: Comparison of the simulated beam profile with the beam's parameter z_0 and q_0 expressed in Table 3.2 for the blue and green lines, while red line is simulated through parameters obtained with the fitting of Figure 3.9. Figure (a) represents the whole beam profile, Figure (b) is a close view of the beam size around the telescope waist, Figure (c) is a close view of the beam size around the target waist.
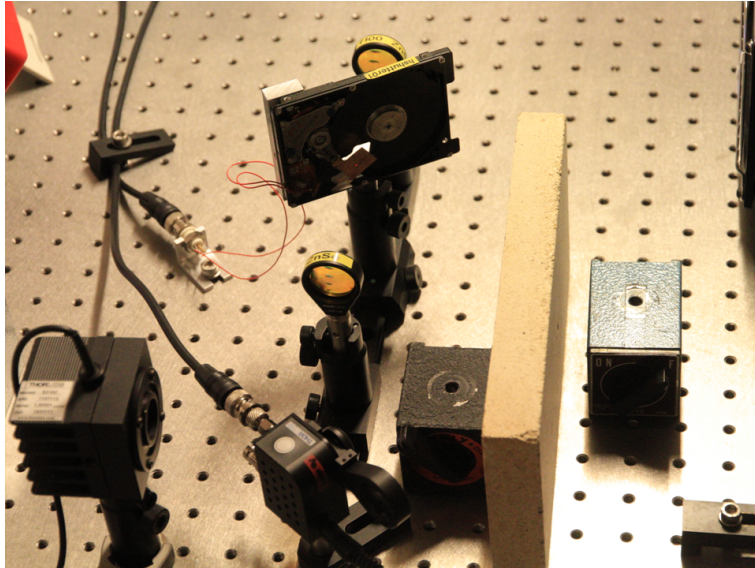
3.3   Hard Drive Shutter

Figure 3.11: Picture of the laser shutters system. The Thorlabs Shutter is open and the laser pointer is focused on the closed flag of the Hard Drive Shutter.

Many laser-based experiments require fast switching of laser beams. There are very fast commercial shutter systems, but they are expensive and require large power supplies. A solution is provided by adapting a standard hard disk device that grants low-cost fast laser shutter [44].

In order to understand how it works, a general overview about its mechanisms is necessary. An hard disk drive is composed of two fundamental parts: the storage area and the read-write head assembly. The read-write head is mounted at the tip of a triangular metallic pivot arm. On the opposite side of the pivot axis there is a tightly wound trapezoidal coil of copper wire between magnets. The coil-magnet assembly is called voice coil actuator (VCA), and it controls the position of the read-write head. Implementing an hard drive shutter, a copper flag is fixed to the pivot arm through epoxy resins, while all other excess components are removed to reduce inertia and maintain balance. A hole in the hard drive holder enables the laser beam to freely pass within the sweep of the shutter arm. An example of the VCA components is presented in Figure 3.12.

The electronics to drive the coil is built[14] based on circuit diagrams conceived in 2007 [45]. This circuit uses discrete components to switch a unipolar power supply through the actuator coil to close the shutter and in the reverse direction to open it. The circuit generates a short high-current transition pulse on each transition. When the input signal switches, the output is reversed and a bipolar capacitor rapidly discharges through the coil.

---

[14]Driving circuits and shutter have been implemented by Bo Melholt Nielsen
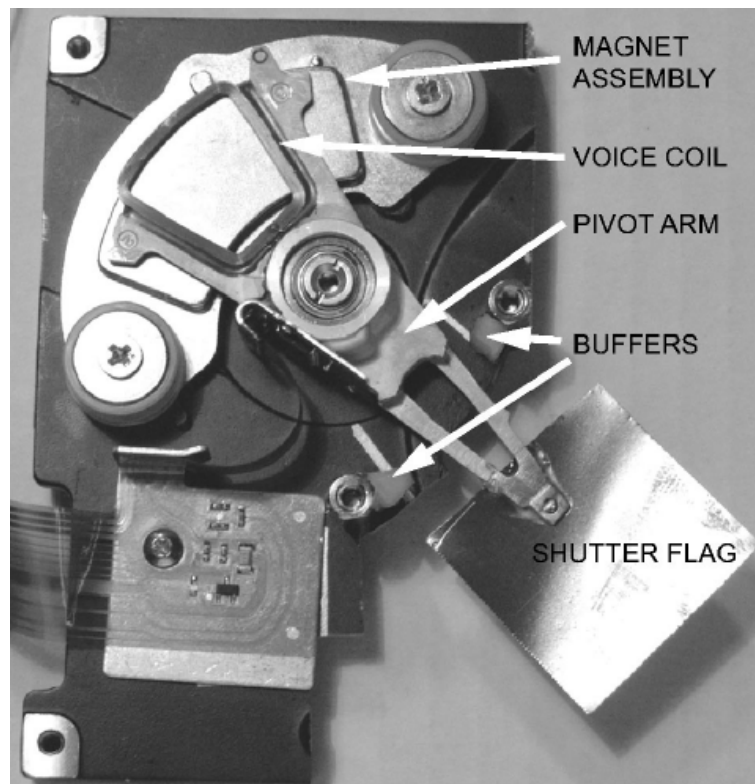
Figure 3.12: Example of the VCA shutter removed to show the voice coils [44].

3.3.1 Hard Drive Shutter characterization

The Hard Drive Shutter is tested to characterize its speed through the CO_2 infrared beam at the telescope waist position. These tests are carried out using the coaligned red laser pointer, instead of the CO_2 laser beam. Using the red laser pointer permits to perform the test at lower powers and with visible light.

In each measurement a photodetector signal records the optical transmission through the shutter, which is compared to the shutter input signal in a LeCroy oscilloscope. An example of this acquisition is shown in Figure 3.13.

The measurement is repeated many times to estimate the switching time through the pointer beam, given by the falling and rising time of the optical transmission signal (Channel 2 in Figure 3.13). An average over the acquisitions returns $\Delta\tau_{pointer} = 95 \pm 4 \ \mu$s. The red pointer beam size at the shutter position is 0.31 ± 0.02 mm. Thus considering the velocity linear in through the beam, the speed of the shutter results $v = 3.3 \pm 0.3$ m/s.
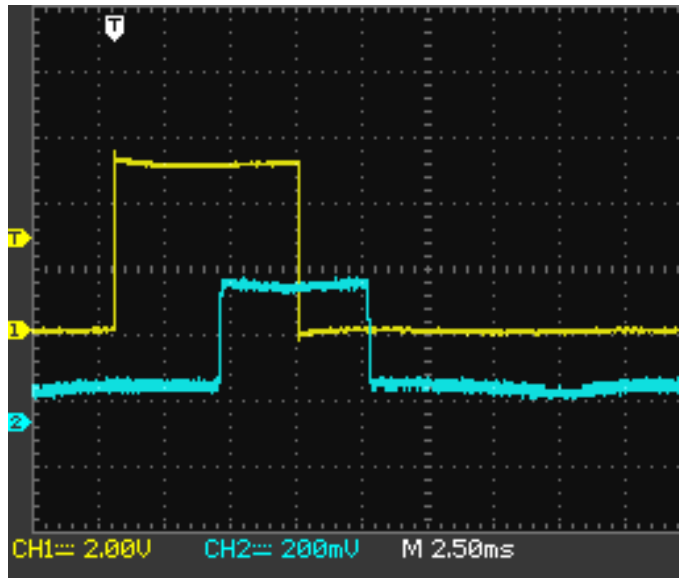
Figure 3.13: Oscilloscope acquisition for a Hard Drive Shutter's test, in order to estimate the flag speed through the beam. In Channel 1 of the oscilloscope (yellow signal) the input signal to the hard drive disk is recorded, while in Channel 2 (blue signal) the optical transmission recorded by a photodetector is presented.

Figure 3.14: Oscilloscope acquisition of shortest pulse achievable by the VCA of the Hard Drive Shutter's test. As in Figure 3.13, in Channel 1 of the oscilloscope (yellow signal) the input signal to the hard drive disk is recorded, while in Channel 2 (blue signal) the optical transmission recorded by a photodetector is presented.

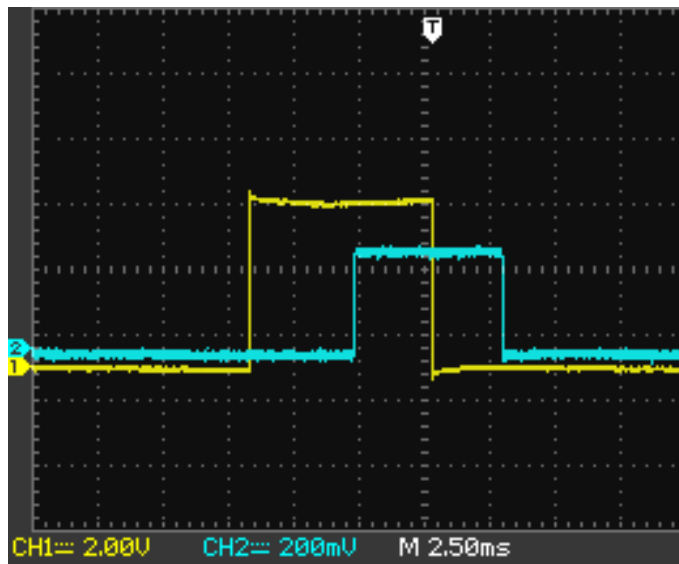The simulated CO_2 beam waist at the telescope position is 0.132 mm (see Section 3.2.3), thus the switching time of the Hard Drive Shutter through the CO_2 laser beam is expected to be $\Delta\tau_{CO2} \approx 40\ \mu$s, more than hundred times shorter than the briefer laser-machining pulse train used in this project. Consequently the switching time through the beam is negligible in the micro-fabrication of the concave structure and no effect of asymmetrical ablation is expected in the surface processing.

A further fundamental property of this shutter is the shortest pulse duration that the VCA can achieve without collateral effects as the pivot arm's bouncing.
The aim of outlining the shortest pulse achievable is reached driving the Hard Drive Shutter with decreasing pulses lengths as input signal, until the pivot arm's starts to behave anomaly. This method yields to an input pulse length of 7.00 ms, as presented in Figure 3.14, coinciding with an optical transmission of 5.64 ms. Using shorter input signals the pivot starts to vibrate or to make a bounce followed by a longer optical transmission window. For this reason no shorter pulse trains are used for the surface laser-machining in this project.

Finally, another characteristic of the Hard Drive Shutter is the time delay between the driving signal and the switch of the pivot arm. This delay also depend on the relative positioning of the flag's edge and the laser beam and results of $\Delta_{delay} = 4.0 \pm 0.1$ ms. This value has to be taken into account in the LabView program that drives the CO_2 laser and shutter's system for imprinting concave structures on the target. This program is presented in the following section.

3.4 LabView driving routine for the setup

A LabView program, implemented for this experiment, controls the driving signals of the CO_2 laser, the shutters' system and the thermal power sensor acquisitions, see Appendix B for the Lab-View interface and script. Each element should be controlled in a precise sequence with defined lengths of time and delays.

The driving signals are provided by a data acquisition device purchased by National Instruments[15] with PWM and TTL outputs. The laser power imping on the power sensor is recorded through a timeline chart. Two bars set up the acceptable power range for the surface processing. The program permits the choice of the duty-cycle and frequency of the laser pumping signal, through a PWM signal, and the duration of the pulses train τ.

As the program runs, if the power constrains are fulfilled, a gating signal starts the machining. This is followed by a TTL signal that opens the Thorlabs' shutter. Its switching is slow compared to the other time scales, thus a time delay $\Delta_1 = 500$ ms is imposed before the following actions. During this period the laser beam is partially reflected by the copper flag on a beam dump. After

---

[15]National Instruments DAQ PCI-6251

this delay, the Hard Drive Shutter input signal is provided with a time length set by the chosen pulses train duration. As expressed in Section 3.3.1, after a second delay $\Delta_2 = 4$ ms the flag edge of the Hard Drive Shutter cross the CO_2 laser beam and shutter opens, consequently the beam reaches the target. Following the τ period, the flag switches again closing the Hard Drive Shutter. Finally another TTL signal stirs up the flipping action of the Thorlabs' shutter. The LabView program is ready for a new pulses train 1000 ms afterwards. This signals sequence is schematically displayed in Figure 3.15.
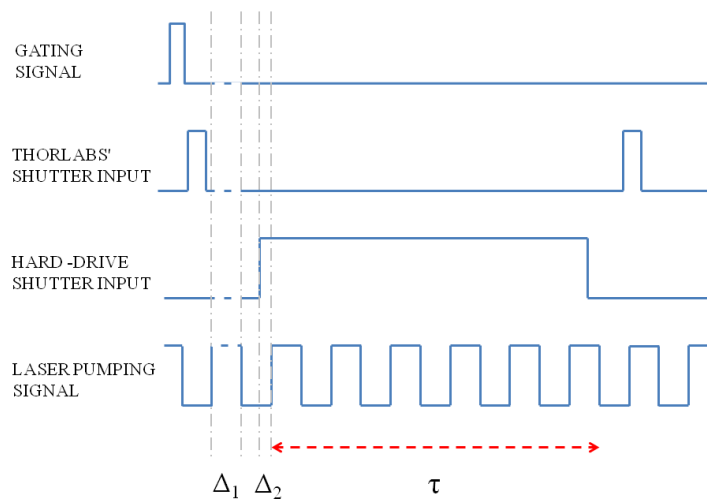
Figure 3.15: Schematic representation of the signals sequence set by the LabView program during the surface processing's pulses train of length τ. The gating signal is provided only when the power constrains are fulfilled. The Thorlabs' Shutter input and the Hard Drive Shutter's one control the shutters switching. Two delays Δ_1 and Δ_2 take into account the finite switching time of the Thorlabs Shutter and Hard Drive Shutter delay (see Section 3.3.1) respectively. Finally the laser pumping signal defines the duty cycle and the frequency of the CO_2 laser beam.

Chapter 4

Laser-machining results

As the aim of the project is a study for the development of a fiber Fabry-Pérot cavity (FFPC), using laser-machined fiber end, a set of concave structures is imprinted through laser ablation on silica plates and on fiber tips. These structure are therefore characterized as a function of the laser parameters in the laser-machining setup. This characterization is necessary to estimate the usability of the depressions as resonators mirrors for a Fabry-Pérot cavity.

In Section 4.1 an introduction on the surface profilometry through AFM is provided. The method of analysis of the concave structure's profiles acquired by means of AFM is presented in Section 4.2. In Section 4.3 the results of the created geometries for different laser parameters are discussed. Finally in Section 4.4 simulations of cavity properties are carried on for resonator assemblies with laser-machined fiber tips subjected to high reflectivity coating.

4.1   Surface profilometry

Surface profilometry has a key role in this project: the imprinted concave structures need to be measured and characterized to estimate their proprieties as resonator mirrors. The AFM is an appropriate choice to investigate the small scale properties of the surfaces.

AFM principles

Atomic Force Microscopy is a surface characterization technique developed in 1988 by Binning et al. [46]. The AFM enables imaging almost any type of surface, probing the surface topography of the sample in high details due to its nanometre-scale spatial resolution.

This technique uses a laser beam deflection system to image the surface topography, see Figure 4.1. More specifically it operates by using a tip attached at the free end of a cantilever, to probe the sample's surface. The laser beam is reflected by the upper part of the cantilever and a photodetec-

tor measures the deflection of the laser beam. The data is thus converted into a topographic image of the probed surface.
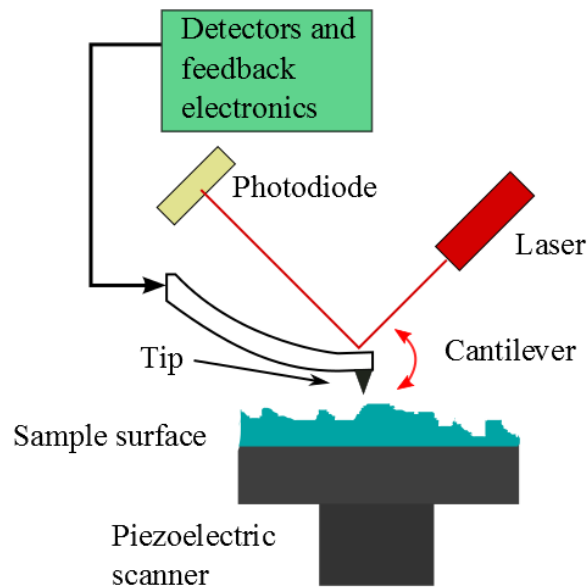

Figure 4.1: Schematic representation of the AFM's principle.

This technique is appropriate for many kind of surface imaging: different types of analysis can be acquired through the different scanning modes. The main three modes the AFM can operate with are described according to the nature of the tip motion [47]: the *contact mode*, the *tapping mode*, also called *semi-contact mode*, and the *non-contact mode*. The contact mode is mainly used to image hard surfaces as the cantilever is scanned relatively to the sample while in contact. In non-contact mode the cantilever probe is moved close to the surface (on Angstroms) and an image of the sample tomography is reconstructed from the van der Waals forces interaction with the surface. In this project the tapping mode has been used. Through this scanning mode the tip periodically touches the surface of the sample. The cantilever is driven to oscillate in a vertical direction near its resonance frequency by a small piezoelectric element mounted in the AFM tip holder. The vibrational amplitude assumes values between 30 and 100 nm [48]. The interaction of forces acting on the cantilever when the tip comes close to the surface (i.e., Van der Waals forces, dipole-dipole interactions, electrostatic forces, etc.) causes the amplitude of this oscillation to decrease as the tip gets closer to the sample. The change in oscillation amplitude are therefore used to identify the surface features. The AFM used in this project is provided by NT-MDT company.

AFM limitations and drawbacks

Even though the AFM is an appropriate profiling technique for concave structure imprinted on silica plates and onto fiber's tips, some limitations and drawbacks have to be taken into account.

First of all, the determination of the surface roughness is limited by an artificial roughness due to the measurement noise. Thus sample's roughness is resolved only if it is bigger than the measurement noise. Some artificial wavy structures are introduced by oscillations of the control loops of the cantilever holder. An estimation of the noise due to these oscillations is given by a Fourier analysis of the recorded topography, see Section 4.2.

The total scan height has some limitations due to the operating range of the piezo control of the cantilever: if the structures are deeper that $5 - 6\ \mu$m, the whole profile cannot be achieved in a single scan and matching different acquisitions is very challenging.

Another significant issue in the measurement is the bending of the sample. In order the acquire the profile, the sample should be fixed to the AFM's holder. This may induce bending and more often tilting of the surface compared to the AFM's coordinate system. In particular tip and sample planes are challenging to be made perfectly parallel. As a consequence, the angle between planes will introduce a spurious height difference along the image. This can be solved by calculating a general plane of the image and then subtracting it from the image raw data [49]. Every scan is therefore subjected to a filter known as plane subtraction, provided by the acquisition program of the AFM[1], in order to compensate for this effect.

Measurements with the atomic force microscope require very slow positioning procedures and the scans themselves are time-consuming.

4.2 Concave structure analysis

Each surface profile obtained through the AFM measurement is analyzed in order to calculate the relevant parameters of the depressions:

- the central radius of curvature *ROC*

- the depth of the structure *d*

- the diameter of the structure *D*

- the surface roughness

These properties are the relevant ones for a resonator assembly.

The analysis of the depressions is achieved through python functions implemented for this specifical investigation, and reported in Appendix C.

---

[1]ND-MDT software

The central radius of curvature and the depth of the structure are obtained fitting the concave structures with a two-dimensional Gaussian function:

$$G(x, y; B, A, x_0, \sigma_x, y_0, \sigma_y) = B - A \cdot \exp\left(-\frac{1}{2}\left(\frac{(x-x_0)^2}{\sigma_x^2} + \frac{(y-y_0)^2}{\sigma_y^2}\right)\right). \qquad (4.1)$$

The fitting results yield to estimations of the central radius of curvature *ROC* and of the depth *d* of the structures respectively as:

$$ROC \approx \frac{\sigma^2}{A} \qquad d = A \qquad\qquad (4.2)$$

In the analysis only the lowest third of the structure profile is taken into account for the fitting. This choice ensures that potential ring-shape structures and spikes due to the deposition of the evaporated material on the depression's boundary are removed from this interpolations: such defects may lower the quality of the fitting. Furthermore it should be noted that the central parts of the craters are the ones of the greatest concerns for the study because they include the extent of the cavity mode on the fiber mirror, which is the relevant size to build an optical resonator.

An example of a concave structure obtained through laser processing in silica is presented in Figure 4.2(a), while the fitting of the depression with a two-dimensional Gaussian is shown in Figure 4.2(b).

The diameter of the depressions *D* is estimated as the distance between the turning points of the height profile, where the shape changes form concave to convex. In the example of Figure 4.2(a) the diameter results $D = 53\ \mu$m.

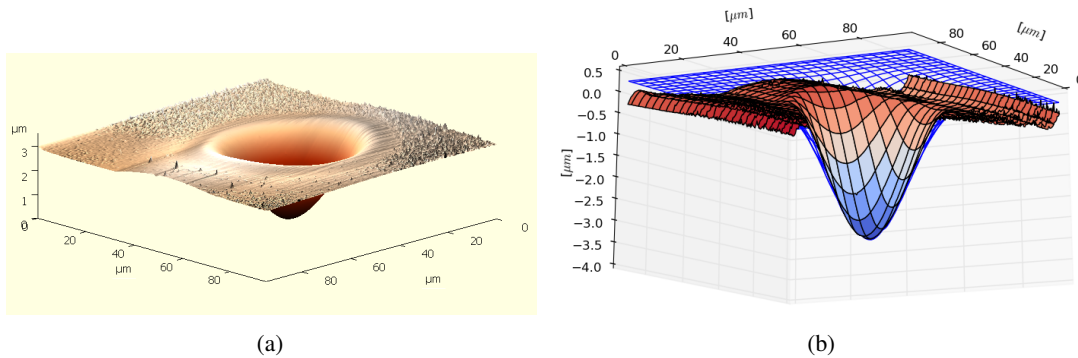(a)   (b)

Figure 4.2: Example of a concave structure obtained with laser processing. This structure is imprinted with a pulse train of $\tau = 30$ ms and duty cycle of 16%. (a) Image of the structure processed through the AFM data analysis program *Image Analysis*. (b) Structure displayed with the 2D Gaussian obtained by the fitting (blue wire-frame).

4.2.1 Fourier analysis

Before the description of the roughness estimation method some consideration on the artificial wavy structures introduced by the control loops of the cantilever have to be discussed. This effect requires a Fourier analysis of the acquired profile.

A Fourier transform is applied to the data in order to filter the depressions in the frequency domains. In particular two different filters are applied for different aims: a high pass filter and a low pass filter.

As far as the high pass filter is concerned, the amplitude spectrum is corrected with Gaussian shaped filters to suppress low frequencies. Through an inverse Fourier transform an estimation of the cantilever noise is achieved as the residual mean square (RMS) relative to a plane area. An example of a high pass filter is presented in Figure 4.3: the original AFM acquisition of a concave structure (a) is transformed in its frequency domain (b), filtered with circular mask to suppress low frequency (d) and inverse Fourier transformed in order to obtain a spatial measurement of the cantilever noise (c). This method is used to study a set of different concave structures obtained with different settings of the laser parameters and yields to a typical cantilever noise of ≈ 2 nm, which is higher than the roughness expected through laser processing in silica [50].

Low pass filters are used in the analysis of the AFM profile acquisitions to compensate the cantilever artificial wavy structures before the interpolation with the 2D Gaussian, however the cantilever noise cannot be neglected in the roughness analysis.
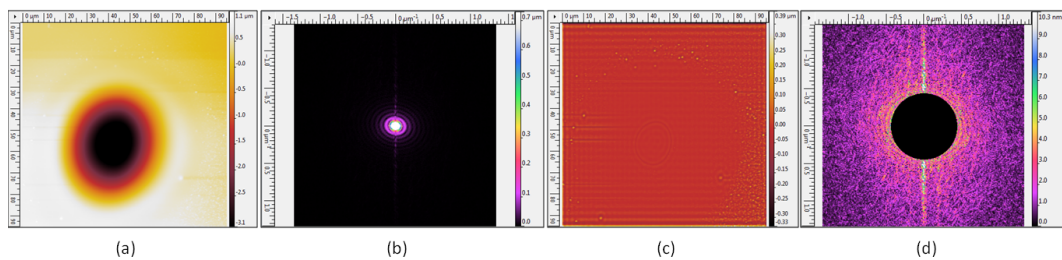
Figure 4.3: Example of high pass Fourier filtering on the AFM acquisition of a concave structure. (a) AFM measurement of laser-machined concave structure imprinted on silica plate. (b) Relative frequency domain of the AFM measurement of the concave structure, obtained through a two-dimensional Fourier transform. (c) Example of AFM data corrected with a high pass filter. (d) Relative frequency domain into which the correction is imposed as circular high pass filter. These images are obtained with Gwyddion modular program.

4.2.2   Roughness

In order to estimate the surface roughness of the concave structure, a two-dimensional 4th-order polynomial background, that accounts for the concave overall shape, is subtracted from a cropped area inside the depression. The surface deviation of this area from a plane, i.e., the RMS of the area, accounts as the surface roughness. This analysis is carried on through the processing functions of Gwyddion, a specialized data visualization and analysis program for scanning probe microscopy.

As the roughness obtained through laser micro-fabrication in silica is assumed to be independent of the laser parameters in the range used in this project [28], only a small set of concave structures is examined. The RMS roughness calculated from residuals in these samples yields to a typical value of 1 nm.

Considering that the estimation of cantilever noise through the Fourier analysis lead to a resolution of the AFM of 2 nm, the roughness analysis shows evidently that the surface roughness is below the measurement noise. Consequently the study infers that the RMS roughness of the concave structures' surface is < 2 nm.

4.3   Concave structure results

A set of concave structures imprinted on silica plates with different settings is used to test the parameters of the processing CO_2 laser beam. Only on a second stage the laser-machining is directed to the fiber's tips.

Two different analysis are carried out: a repeatability test and the study of different settings.

Repeatability test

First of all the repeatability of laser-maching process is tested through a series of repeated laser processing using three different settings.

- 6 concave structure are imprinted for a train pulse $\tau = 500$ ms, with duty-cycle of 12.5% and with a power range of 0.951 ± 0.001 W.

- 5 structure are imprinted for a train pulse $\tau = 50$ ms, with duty-cycle of 14% and with a power range of 1.14 ± 0.2 W.

- 7 structure are imprinted for a train pulse $\tau = 5.6$ ms, with duty-cycle of 18% and with a power range of 1.48 ± 0.2 W.

The geometrical parameters of the structures are compared for each settings in Figure 4.4, resulting in Table 4.1.
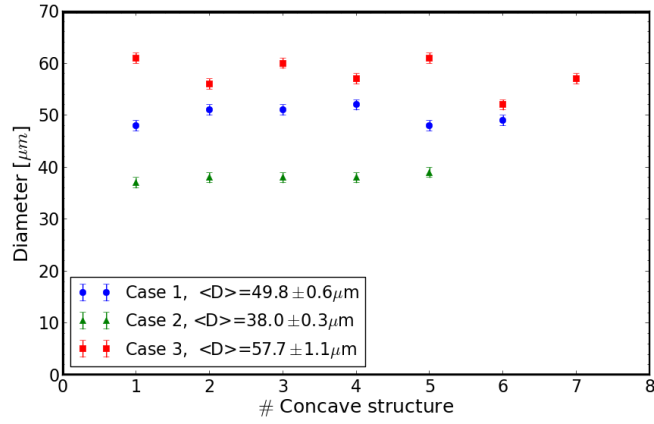
(a)
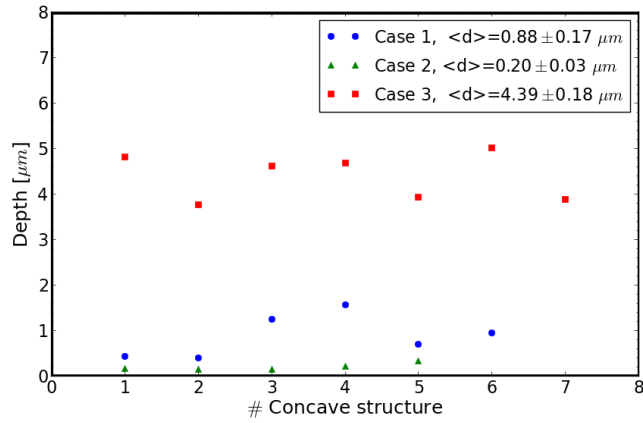
(b)
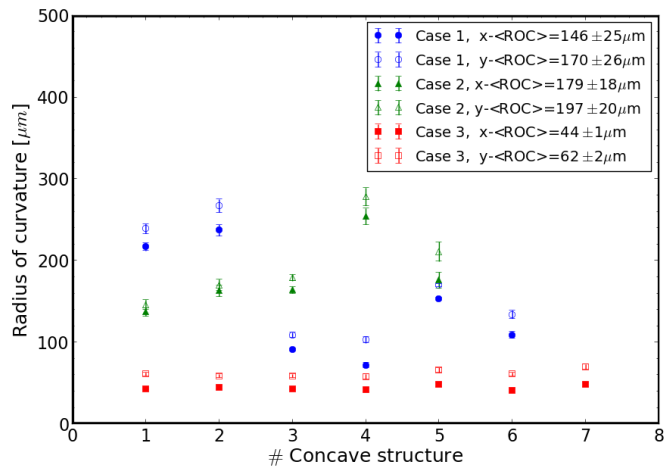
(c)

Figure 4.4: Results of the repeatability test on three different settings of the laser power and duration of the pulse trains for the processing of silica plate. Case 1: Power=(0.951±0.001) W and $\tau = 500$ ms. Case 2: Power=(1.14±0.02) W and $\tau = 50$ ms. Case 3: Power=(1.48±0.02) W and $\tau = 5.6$ ms. The graphs present the measured diameters (a), the structures depths (b) and the radius of curvature in the $x-$ and $y-$ direction(c) recording the average value in each settings.

It is evident from Figure 4.4 that all the settings taken into account present a large dispersions in the structural properties of the imprinted depressions, although these results are comparable to the ones obtained in Ref. [20]. This dispersion appears to decrease with higher powers and for shorter machining pulse trains. This result was expected considering the power fluctuations of the CO_2 laser used in the project, fluctuations that are enhanced when the device is driven at lower power. Another important point to remark is that the radius of curvature in the $y-$direction is larger than the one in the $x-$direction in every structure. This is a clear evidence of a residual ellipticity of the CO_2 beam at the target position, even after the optimization discussed in Chapter 3.

	D	d	$x - ROC$	$y - ROC$
0.951 ± 0.001 W $\tau = 500$ ms	$49.8 \pm 0.6\ \mu m$ (1%)	$0.88 \pm 0.17\ \mu m$ (19%)	$146 \pm 25\ \mu m$ (17%)	$170 \pm 26\ \mu m$ (15%)
1.14 ± 0.02 W $\tau = 50$ ms	$38.0 \pm 0.3\ \mu m$ (1%)	$0.20 \pm 0.03\ \mu m$ (15%)	$179 \pm 18\ \mu m$ (10%)	$197 \pm 20\ \mu m$ (10%)
1.48 ± 0.02 W $\tau = 5.6$ ms	$57.7 \pm 1.1\ \mu m$ (2%)	$4.39 \pm 0.18\ \mu m$ (4%)	$44 \pm 1\ \mu m$ (2%)	$62 \pm 2\ \mu m$ (3%)

Table 4.1: Average value of diameter D, depth d and radius of curvature ROC in the $x-$ and $y-$directions for the different settings recorded with the relative percent error shown in brackets.

Different settings

The geometrical properties of the depressions are strongly dependent on the laser parameters of power and pulse train length τ. The following analysis thus investigates a set of depressions machined in a silica plate with a broad range of irradiation times and intensity, see Table 4.2. The laser power is chosen between 958 mW and 1.675 W, while the pulse trains have lengths of $\tau = 10$ ms to 500 ms.

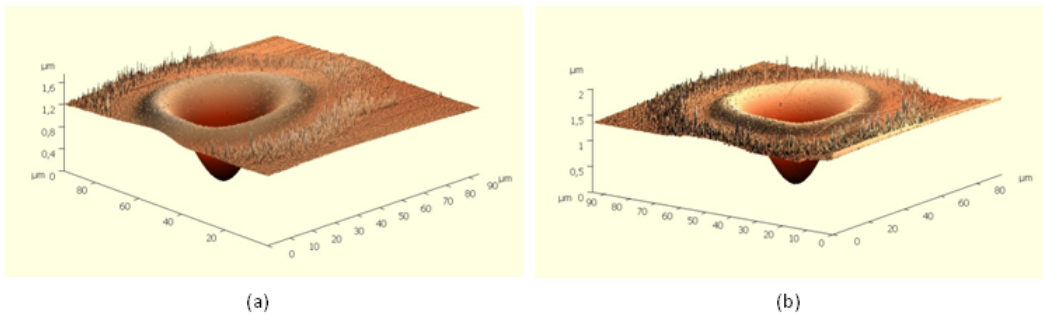

(a)   (b)

Figure 4.5: Examples of imprinted depressions that present ring shape structures on the top. (a) Pulse train length $\tau = 450$ ms (b) Pulse train length $\tau = 500$ ms.

The acceptable ranges of laser parameters in silica processing are limited by two physical limits. The surface smoothing process is slower than the melting and resolidification which occur for very short pulse trains at high intensity. Long pulse trains on the other hand produce a global contraction into a convex shape because the melted layer expands far into the volume [51]. This regime is announced by the ring shape structures that are already present on the top of the depressions imprinted for the longest pulse trains used in this project, see Figure 4.5.

The study concentrates on the relation between d and ROC which are the parameters of interest for a resonator assembly, as they are critical in defining the mode size in the cavity, the cavity length and the clipping losses $\mathcal{L}_{cl}$. The nonlinear power dependence of the laser-machining process is evident from Figure 4.6. It is clearly visible that generally the depths get larger with raising intensities and longer pulse length, while the radius of curvature has an opposite behaviour. The structure diameter can be made bigger with higher irradiation intensities applied over longer timescales.

	10ms	20ms	25ms	30ms	40ms	50ms	75ms	100ms
0.975±0.005W								
1.035±0.005W								
1.095±0.005W								x
1.185±0.005W			x	x	x	x	x	x
1.445±0.005W	x	x		x	x	x	-	-
1.535±0.005W	x	x	x		-			
1.675±0.005W	-							
	150ms	200ms	250ms	300ms	350ms	400ms	450ms	500ms
0.975±0.005W		x	x	x	x	x	x	x
1.035±0.005W	x	x		x	x	x		
1.095±0.005W	x	x	x	x	x	-		
1.185±0.005W	-							
1.445±0.005W	-							
1.535±0.005W								
1.675±0.005W								

Table 4.2: The combinations of power and pulse trains' length used to imprint concave structures are marked in the table. "x" represents analyzed depressions while "−" symbolizes imprinted depressions that are too deep to be measured with the AFM.

In conclusion by adjusting the laser parameters of power and machining pulse length, different conformations of concave structures can be achieved to implement an optical resonator. Simulations of the optical cavities's properties for different conformations are presented in Section 4.4.
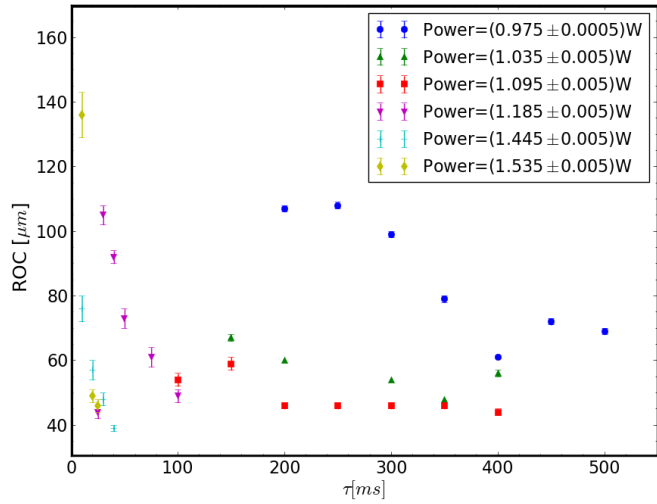
(a)
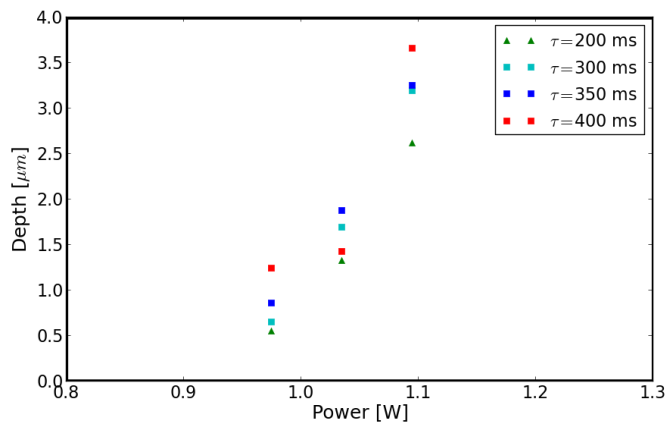
(b)
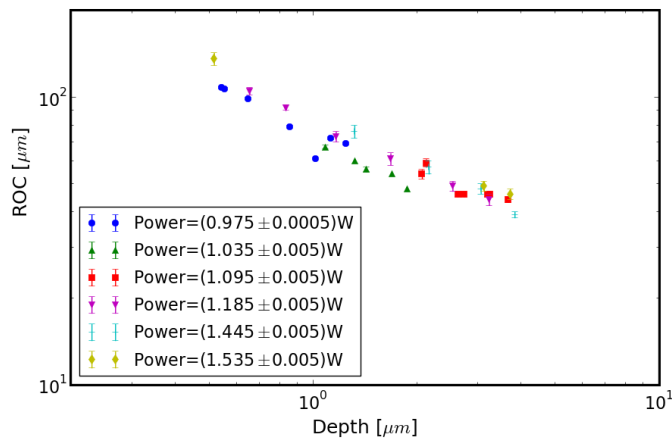
(c)

Figure 4.6: Set of concave structure imprinted with parameters of Table 4.2.(a) Plot of the radius of curvature *ROC* as a function of the pulse train length τ for different power. (b) Plot of the depth *d* as a function of the laser power fr different pulse length. (c) Plot of radius of curvature *ROC* as a function of the depth *d*.

4.3.1 Concave structure on fibers

A set of single mode fibers and multimode fibers has been processed during this project. In particular, as mentioned in Section 3.1, single mode fibers have diameter of 125 μm, while multimode fibers of 225 μm. Before the laser processing each fiber is stripped from the buffer coating and cleaved through a mechanical cleaver[2]. The fiber end facet surface is submitted to an inspection with the microscope camera in the laser-maching setup in order to check the quality of the cleaving process. If the cleave is acceptable the fiber is processed by means of the CO_2 laser beam.

The fibers' concave structures are prepared with settings previously tested on the silica plates. However the profile diameters of the craters are expected to be slightly and systematically larger than the one imprinted on the silica plates due to the boundary conditions set by the cylindrical geometry of the fibers. The constrains of the transverse heat flow provokes a heat accumulation that yields to an enlarged area which is melt and evaporated. This effect should be enhanced in the thinner single mode fiber. Unfortunately the AFM holder to measure fibers tip was not available during the project due to some mechanical problems, thus the dependency of the concave structures on the laser parameters and on the fiber size has been roughly verified through a quality analysis of the microscope's images of the fiber tips.
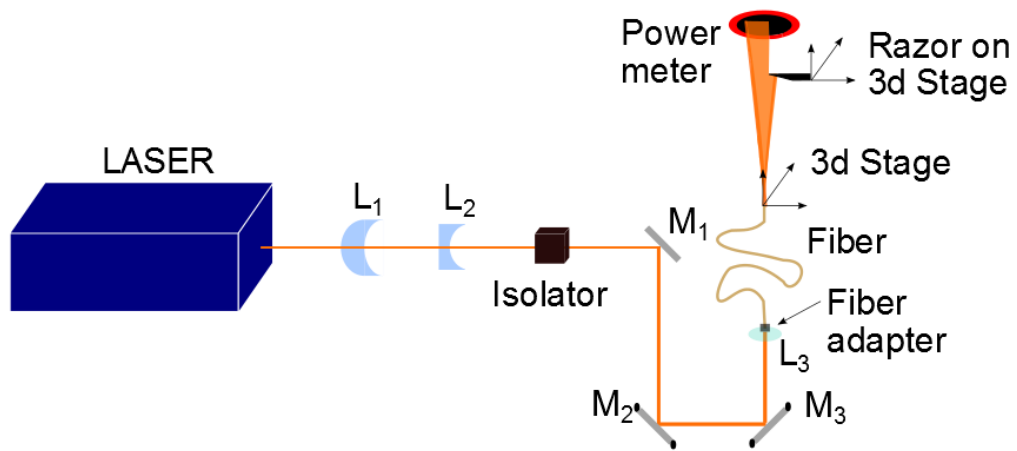
Figure 4.7: Schematical rappresentation of the setup implemented to couple a laser beam into single mode optical fiber and try to estimate the radius of curvature of the imprinted fiber tip. *L* symbolizes lenses. L_1 and L_2 are cylindrical lenses inserted to correct the ellipticity of the beam and makes the beam size suitable for the isolator. *M* represents mirrors, in particular M_2 and M_3 are used for the fine alignment necessary to couple into the fiber. Two translational stages are used to set the position of the concave fiber tip and of the razor to measure the beam size.

---

[2]FUJIKURA CT-10

An attempt of estimation of the fiber tips curvature has been carried out considering the lensing effect of fiber's tip concave curvature on a large scale, as in Figure 4.7. The beam provided by laser diode[3] at 637 nm has been coupled into different single mode fibers. The profile of the beam output from the concave fiber tips has been measured and compared for various fibers. However, the difficulty of setting a fixed coordinate reference for the concave structure's (i.e., the diverging lens) position with high precision prevents achieving accurate estimations.

4.4   Cavity simulations

Given the results of the structural properties for the depressions imprinted with different setting, some simulation are carried out for the attributes of cavities that are going to be implemented with these depressions on fiber end facets. As introduced in Section 2.2 the cavity considered for this project consists of a plane dielectric mirror onto which nanodiamonds are spin-coated and of an optical fiber facet machined to yield a concave imprint. An NV center of the nanodiamonds is excited by a 532 nm laser beam through the plane mirror, while single-photon emitted by the NVs are collected through a single mode fiber.
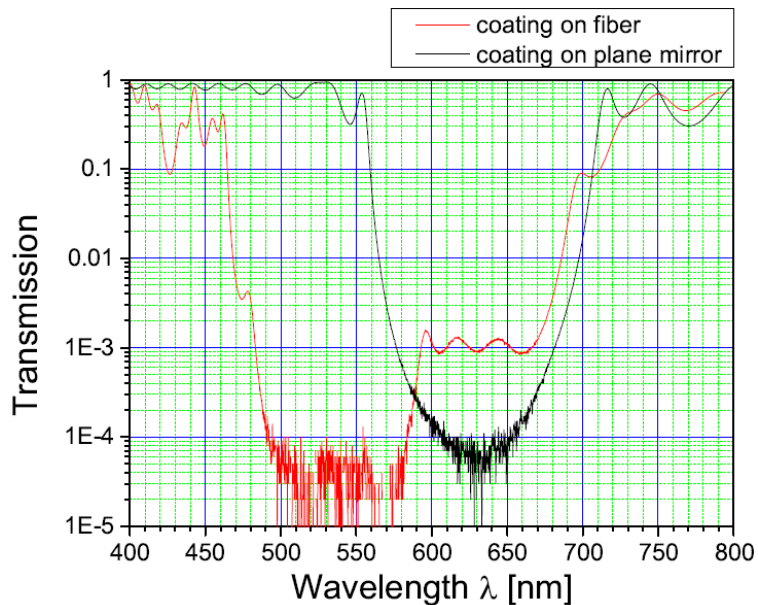

Figure 4.8: Example of trasmission of the multilayer coatings on plane mirror and on fiber used for a FFPC.

In order to obtain a cavity, after the laser processing, the fiber end facet and the plane mirror should be coated with a high performance dielectric multilayer coatings. These coating are going

---

[3]Toptica Photonics DL 100 L_03050

to be performed by LAYERTEC. The transmission properties of the two coating are presented in Figure 4.8. In particular the expected reflectivity for the fiber coating is going to be $\mathcal{R}_2 \approx 99.9\%$ at 637 nm, the NV centers ZPL, and $\mathcal{R}_2 > 99.998\%$ at 532 nm. The plane mirror is going to present $\mathcal{R}_1 > 99.994\%$ at 637 nm and $\mathcal{R}_1 < 0.1\%$ at 532 nm. These properties are necessary to have a good cavity at 637 nm and avoid to suppress the NV's ZPL with the 532 nm beam collected by the fiber.

Another critical aspect of multilayer coating concerns the cavity length. It has been proved that the presence of a multilayer coating influences the effective length of a cavity [52]. The leakage of the cavity mode in the mirrors stacks gives rise to an additional phase shift at the coatings, causing an additional contribution to effective cavity length. As a consequence the cavity length considered in the simulation is

$$L_{eff} = L_{Geom} + \alpha_{ml}\frac{\lambda_{ZPL}}{2}. \tag{4.3}$$

where L_{Geom} is the geometric cavity length and $\alpha_{ml} = 1.6$ accounts for multilayer coating effect. The simulations are performed only for resonant cavity lengths so that L_{Geom} is an integer number of $\lambda_{ZPL}/2$ and should at minimun equal to the concave structure depth. In the simulation six different concave structure analyzed in Section 4.3 are taken into account as recorded in Table 4.3 with the relative properties.

	Power	τ [ms]	D [μm]	d [μm]	ROC [μm]
Case 1	1.535 ± 0.005W	10	41	0.52	136
Case 2	1.445 ± 0.005W	30	53	3.05	46
Case 3	1.185 ± 0.005W	50	39	1.16	73
Case 4	1.095 ± 0.005W	250	54	2.73	40
Case 5	0.975 ± 0.005W	500	51	1.24	69
Case 6	0.975 ± 0.005W	200	45	0.51	107

Table 4.3: Settings of the laser-machining setup and structural properties of the depressions used to simulate cavities.

Simulations of the Purcell factor of the cavity and of the coupling efficiency with the fiber as function of the cavity length are performed through python routines. All the relations between the different cavity variables are expressed in Section 2.2. In particular the Purcell factor is estimated through Equation 2.40, as

$$F_P = \frac{6\lambda^2}{\pi^3}\frac{\mathcal{F}}{w_0^2}. \tag{4.4}$$

which express this parameter in case of a single atom in a FFPC.

The finesse of the cavity, calculated as

$$\mathcal{F} = \frac{2\pi}{\mathcal{L}} = \frac{2\pi}{\mathcal{S} + \mathcal{L}_{cl} + T_1 + T_2},$$
(4.5)

is estimated taking into account the scattering losses of the cavity $\mathcal{S}$ and the clipping losses $\mathcal{L}_{cl}$. The scattering losses arise from the roughness of the mirror's surface which, in these simulations, is estimated to be 0.2 nm, i.e., the typical value reached with laser-machining on silica. The clipping losses have a dependence on the cavity length through the size of the cavity mode on the fiber mirror. However the contribution of the clipping losses is negligible compared to the scattering losses and the transmission losses. That results in a typical finesse of around 5500 for each cavity simulated.

The probability for the emission of a photon via the cavity, in strong coupling regime, in adiabatic approximation, and for sufficiently long time interval, is [28]

$$P_{em} \approx \frac{F_P}{1 + F_P}.$$
(4.6)

However not all the single-photons emitted from the cavity are transmitted, due to scattering and absorption losses at the mirrors, or they are transmitted through the "wrong" resonator mirror. Therefore the probability for efficient extraction of an emission event accounts as

$$P_{exctraction} = \frac{T_2}{T_1 + T_2 + \mathcal{L}_1 + \mathcal{L}_2}.$$
(4.7)

where $\mathcal{L}_i$ represents the losses in the ith resonator mirror.

Finally another limit to the single-photon collection from the FFPC is connected to the matching efficiency of the resonator mode with the fiber mode. The coupling efficiency ε with the fiber mode is evaluated, as in Equation 2.33, as

$$\varepsilon = \frac{4}{\left(\frac{w_f}{w_m} + \frac{w_m}{w_f}\right)^2 + \left(\frac{\pi n_f w_f w_m}{\lambda R}\right)^2}.$$
(4.8)

thus taking into account possible mismatch between the wavefront curvatures. The size of the transverse fiber mode used in the calculations is $w_f = 4 \ \mu$m, i.e., the mode size of single mode fiber imprinted in this project.

The overall probability of photon emission into the cavity and subsequent extraction via the single mode fiber is hence

$$P_{tot} = P_{em} \cdot P_{exctraction} \cdot \varepsilon.$$
(4.9)
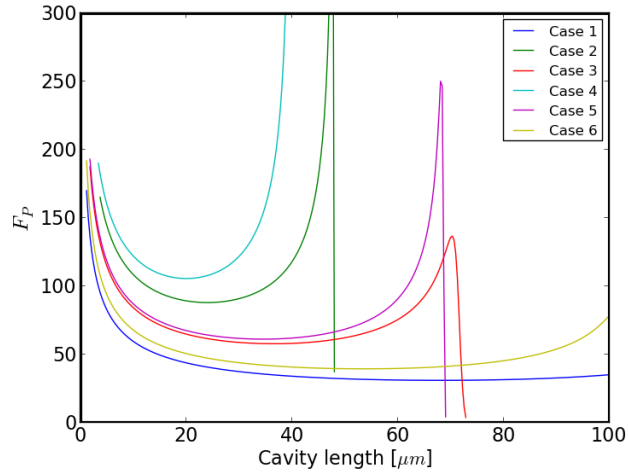
(a)
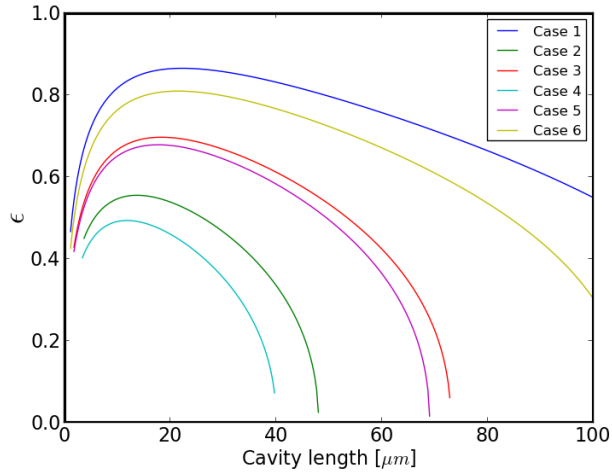
(b)
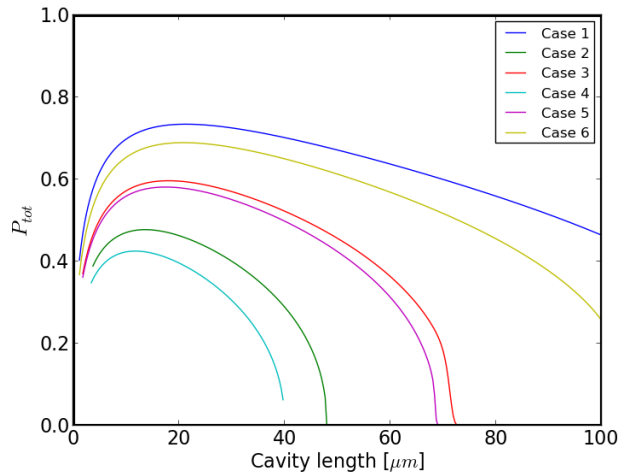
(c)

Figure 4.9: Simulations of the Purcell factor F_P (a), the coupling efficiency ε with single mode fiber (b), and the probability of photon emission into the cavity and subsequent extraction through the single mode fiber (c) for a FFPC implemented with the different concave structure on the fiber end facet presented in Table 4.3. Only resonant cavity lengths are considered in the simulations.

Figure 4.9 clearly shows that, taking into account a FFPC in strong coupling regimes with a single atoms, the concave structures properties influences the most the overall probability P_{tot} by means of the coupling efficiency into the single fiber mode. The simulation in 4.9(c) moreover proves that the overall probability of photon emission into the cavity and subsequent extraction via the single mode fiber is higher for imprinted concave structure with lower depth and higher radius of curvature.

In conclusion from the simulation plots in Figure 4.9 it is evident that, using laser-machined fiber's tips with multilayer coating, it is possible to implement FFPC to enhance the zero phonon line emission of NV center in nanodiamonds, spin coated on the resonator plane mirror. These optical resonators are high finesse cavities with high Purcell factor and good coupling efficiency into single mode fibers.

Chapter 5

Experimental results on cavities and Nitrogen-vacancy centers

This project aims to study the implementation a FFPC to enhance single-photon emission from NV centers. In order to get accustomed with cavities and NV centers, some experiments with aligning cavities and detecting NV centers are performed and presented in this Chapter.

Section 5.1 presents the realization of a macroscopic cavity tuned by a piezoelectric actuator. Particular attention is paid to the implementation of the setup (Section 5.1.1), to the resonator stability conditions (Section 5.1.2), and finally to the estimation of the cavity's finesse (Section 5.1.3). In Section 5.2 the method of identification of NV centers is described. The setup used for this investigation is introduced in Section 5.2.1, while the analysis of a sample with spin-coated nanodiamonds is presented in Section 5.2.2.

5.1 Macrocavity

A macroscopic optical cavity is implemented in this project and coupled to a laser beam at 637.0 nm. The cavity length is tuned through a piezoelectric actuator recording the reflection spectrum of the resonator. The analysis of the spectrum, as shown in the following sections, leads to an estimation of the cavity finesse that is comparable to its expected value from theory.

5.1.1 Setup

The experimental setup is shown in Figure 5.1. A Toptica Photonics laser diode[1] provides a light beam at 637.0 nm. A crucial point in the setup is the presence of an optical isolator, which is

---

[1] Toptica Photonics DL100 L‗03050

required to protect the laser cavity from back reflections. A careful control of back reflections is particularly crucial for laser diode as light would be coupled into the diode and cause fluctuations in power and wavelength [53]. Therefore two cylindrical lenses (i.e., L_1 and L_2) provided by Thorlabs, shape the laser beam to compensate for its ellipticity and to make it of the proper size to fit into the optical isolator[2].
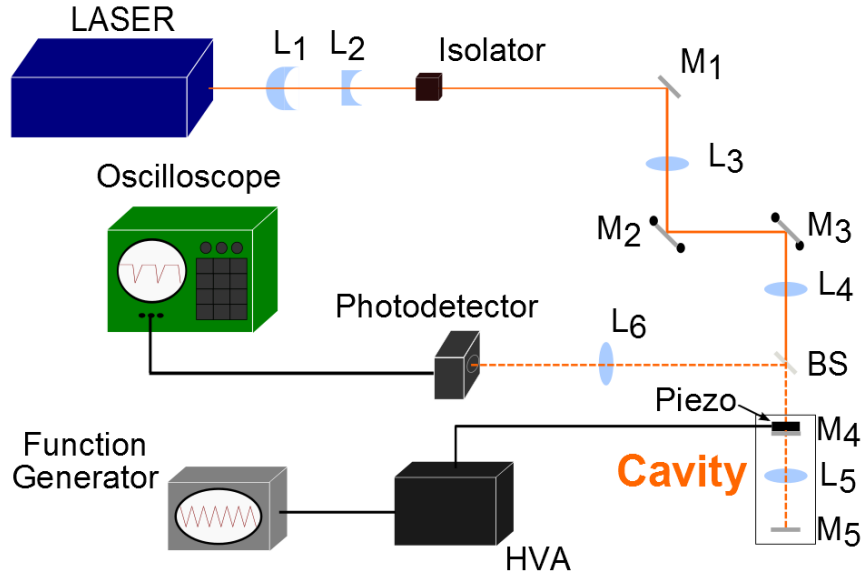

Figure 5.1: Experimental setup realized to implement a macroscopic cavity. L refers to lenses, M to mirrors, BS represents a 50/50 beam splitter, HVA is a high voltage amplifier. Piezo identifies the piezoelectric actuator attached to mirror M_4.

The laser beam is aligned through a mirrors system to a macroscopic cavity. In particular, mirrors M_2 and M_3 are used for the fine adjustment of beam alignment with the cavity, thus they are set on kinematic mounts which provide fine angular adjustment.

The cavity is composed of two plane mirrors (referred to as mirrors M_4 and M_5 in Figure 5.1) with a spherical lens in between (i.e., lens L_5). The lens is characterized by focal length $f = 50$ mm and features a multilayer coating that grants reflectivity and absorbance lower than 0.25% in the spectral range of 600-1050 nm. Mirror M_4 presents reflectivity $\mathcal{R} = 95.2\%$ and transmission $\mathcal{T} = 3.1\%$, while mirror M_5 is designed to have reflectivity $\mathcal{R} = 99.4\%$ at 637.0 nm. The distances between these elements are discussed in more details in Section 5.1.2.

The cavity length is tuned by means of a piezoelectric actuator of lead zirconate titanate (PZT) [54]. Mirror M_4 is attached through epoxy resins to a ring shaped PZT, which is itself set onto a massive mounting structure. A triangular signal, provided by a signal generator and am-

---

[2]Thorlabs IO-3D-633-PBS

plified by a high voltage amplifier, drives the oscillations of the piezo element, tuning the position of M_4.

The output signal emitted from the resonator is directed through a beam splitter onto a photodetector[3] connected to an oscilloscope.

5.1.2 Cavity stability

Before the implementation of the cavity an estimation of the expected stability is derived. In Figure 5.2 a schematic representation of the sequence of mirror and lenses equivalent to a cavity round-trip of the light is displayed. It is supposed that the light beam starts its propagation from the coupling mirror M_4, propagates for a distance d_1 until lens L_5, it propagates for a distance d_2 up to mirror M_5, reflects back to the lens and it is focused down again into mirror M_4 and reflected, completing one round-trip.
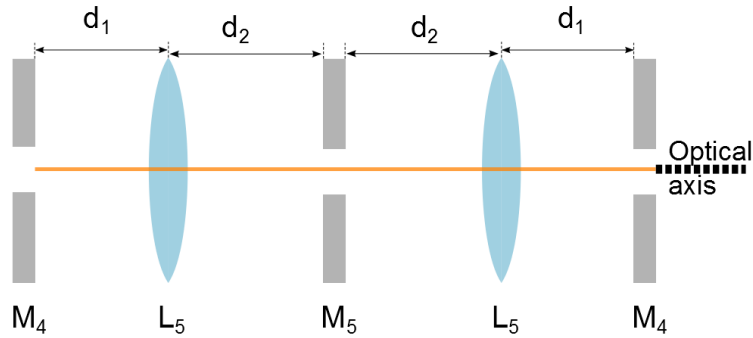
Figure 5.2: Schematic representation of the sequence of mirrors and lenses equivalent to a resonator round-trip of light.

Using the ray matrices defined in Section 2.1.1 for the propagation of a Gaussian beam through optical elements, the ABCD matrix of the system for a complete round-trip results

$$\begin{pmatrix} A & B \\ C & D \end{pmatrix} = \begin{pmatrix} 1 & d_1 \\ 0 & 1 \end{pmatrix} \begin{pmatrix} 1 & 0 \\ -\frac{1}{f} & 1 \end{pmatrix} \begin{pmatrix} 1 & d_2 \\ 0 & 1 \end{pmatrix} \begin{pmatrix} 1 & d_2 \\ 0 & 1 \end{pmatrix} \begin{pmatrix} 1 & 0 \\ -\frac{1}{f} & 1 \end{pmatrix} \begin{pmatrix} 1 & d_1 \\ 0 & 1 \end{pmatrix}, \quad (5.1)$$

where f=50 mm is the focal length of lens L_5 and d_1 and d_2 are respectively the distances from M_4 and M_5 to the lens, as in Figure 5.2.

---

[3]Thorlabs PDA36A

The stability criteria for optical cavities, introduced in Equation 2.21, states that

$$-1 < \frac{A+D}{2} < 1, \tag{5.2}$$

thus applying this rule to the ABCD matrix of the system yields to

$$-1 < \frac{f^2 - 2f(d_1 + d_2) + 2d_1 d_2}{f^2} < 1. \tag{5.3}$$

Taking into account $d_1 = 95$ mm and $d_2 = 100$ mm results in

$$\frac{A+D}{2} = 0.8, \tag{5.4}$$

that fulfils the stability criteria. These distances between the optical elements are therefore used to realize the macroscopic cavity.

5.1.3 Cavity spectrum and finesse

The cavity has been successfully aligned resulting in the characteristic reflection spectrum of an optical resonator, recorded in Figure 5.3. This plot is acquired through the oscilloscope as the piezoelectric actuator is scanning the cavity length. The intense resonances correspond to fundamental longitudinal cavity mode, while weak resonances correspond to higher order modes.

The finesse of the resonator has been estimated both theoretically from the expected losses $\mathcal{L}$ and from the acquired spectrum. As in Equation 2.29, the finesse can be calculated as

$$\mathcal{F} = \frac{2\pi}{\mathcal{L}}, \tag{5.5}$$

where $\mathcal{L}$ represents the cavity losses.
Taking into account the absorbance and transmissions of the resonator mirrors and the optical density of the cavity lens, expressed in the setup presentation in Section 5.1.1, the Finesse results

$$\mathcal{F} = \frac{2\pi}{\mathcal{T}(M_4) + \mathcal{T}(M_5) + A(M_4) + A(M_5) + 2 * A(L_5)} \approx 106, \tag{5.6}$$

where $\mathcal{T}(i)$ represents the transmission of the ith optical element and A(i) its absorbance.
From the experimental point of view, the finesse is defined as ratio between the free spectral range (FSR) and the FWHM of the main resonance mode, as expressed in Equation 2.18:

$$\mathcal{F} = \frac{\Delta\lambda}{\delta\lambda}. \tag{5.7}$$
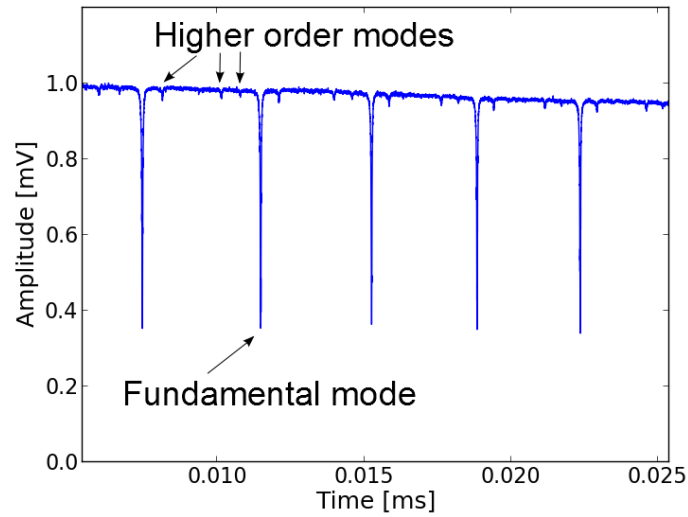
Figure 5.3: Reflection spectrum output from the cavity, scanned by means of a piezoelectric actuator.
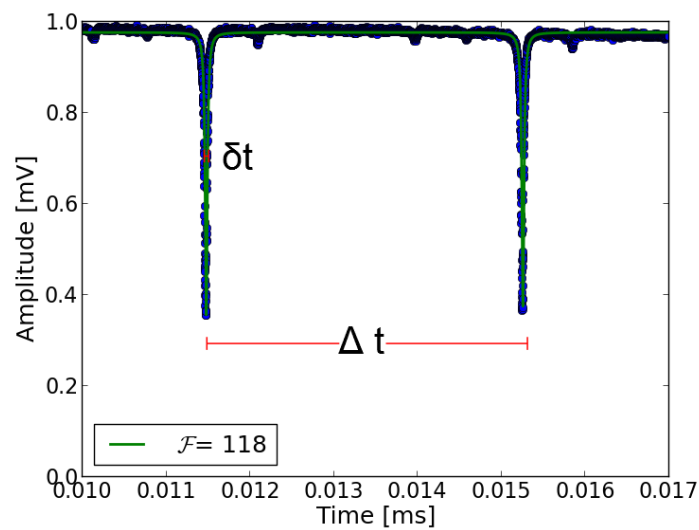
Figure 5.4: Reflection spectrum output from the cavity scanned over a full FSR The green line is the Lorenztian fis of the resonances.

As the piezoelectric actuator is operated in a linear regime and the cavity length directly depends on the voltage signal applied to the piezo element, it is possible to assume a linear dependence between the recording time and the shift in the cavity length.

That yields to assume [55]

$$\mathcal{F} = \frac{\Delta\lambda}{\delta\lambda} = \frac{\Delta t}{\delta t}. \tag{5.8}$$

Analysing the spectrum through Lorentzians (green line) fitted to the resonance peaks, as in Figure 5.4, gives an estimation of the Finesse as $\mathcal{F} = 118.2 \pm 0.5$. This value is comparable to the theoretical one calculated from the expected losses with a difference of 11%.

5.2 Nitrogen-vacancy center's single-photon emission

This project aims to implement a cavity to enhance the single-photon emission of NV centers. Therefore during the project an important focus is the identifications of the NV centers emission. In a home-built scanning confocal microscope [56], the fluorescence emission of a sample with nanodiamonds spin coated on it is measured. The results allow locating NV centers and verifying their properties as single-photon sources.

5.2.1 Setup

The investigation on NV centers is carried out on a standard scanning confocal microscope [57] using an oil immersion objective with a numerical aperture of 1.4, as illustrated in Figure 5.5.
A 532 nm continuous wave laser is used to excite the NV centers. The fluorescence emission from the sample is collected by the objective and split by a symmetric beam splitter. One beam splitter output is directly imaged on a avalanche photo diode (APD1), while the other optical channel can be decoupled by a galvanometric mirror before being detected by a second avalanche photo diode (APD2). Before photo-detection, the light of either optical path is band-pass filtered with a transmission window between 647 nm and 785 nm to remove any residual pump light. The system of APD1 and APD2 together with the symmetric beam splitter composes a standard Hanbury Brown and Twiss setup [58] for measuring the second order correlation function $g^{(2)}(\tau)$. All time-correlated data were recorded with a time to amplitude converter (TAC) provided by PicoQuant. A spectrum analyser can be inserted in the optical path of APD2 to record the emission spectrum.

The sample for this experiment was prepared on a fused silica substrate with thickness of 0.14 mm. The substrate was mounted onto a spinner with on top of it a solution of polyvinyl alcohol (PVA) [59] containing nanodiamonds with size < 50 nm [4]. The sample was spun at 2000 rpm (revolutions per minutes) for 120 s in order to obtain a layer of PVA of nominal thickness of 500 nm. Only a few of the nanodiamonds contain single NV centers and are therefore optically active.
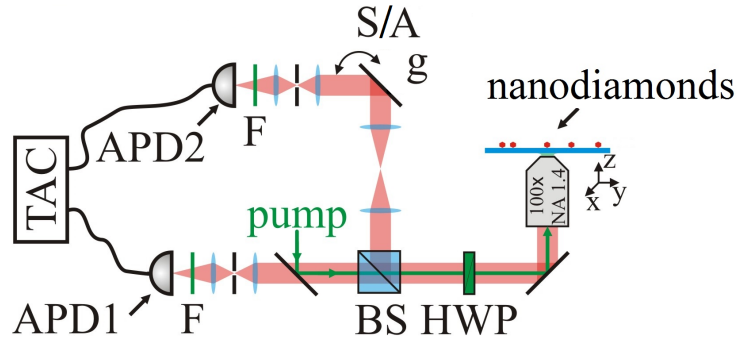
---

[4]MicrodiamtAG

Figure 5.5: Experimental setup for NV centers investigation [18]. The sample consists in nanodiamonds spin coated onto a fused silica slit. The acronyms are: HWP - half waveplate, BS - 50/50 beam splitter, g - galvanometric mirror, S/A - spectrum analyser, F - band-pass filter, APD1 and APD2 - avalance photo detector channel 1 and 2, TAC - time to amplitude converter. Pump represents the excitation light source at 532 nm.

5.2.2 Results on Nitrogen-vacancy centers

In order to determine the possible positions of NV centers, at first a scan of the fluorescence collected with APD1 through the glass plate is performed. The sample is moved through piezo actuator stages in the plane normal to the pumping laser beam.

NVs are excited driving the pumping laser at 1 mW. NVs appear as bright fluorescence spots on a low background. However it is necessary to identify whether the bright centers are NV centers or any other fluorescence source such as other crystallographic defect or impurities in the PVA layer.

A first investigation is performed by continuously exciting the spot while scanning the image plane using the galvanometric mirror as shown in Figure 5.6 and therefore measuring the signal in the bright spot. NV centers should present a strong and stable signal [11, 34] unlike the impurities in the PVA layer.

A second test is performed through a measurement of the second order correlation function $g^{(2)}(\tau)$. The Hanbury Brown and Twiss setup splits the light in two optical channels and record the number of coincident photo-detection events at the different APDs with time difference τ. This measurement is the usual method to identify a single-photon source.

As discussed in Appendix A, an ideal single-photon source is characterized by a second order correlation function $g^{(2)}(\tau = 0) = 0$. This calculation however considers an ideal measurement, while $g^{(2)}(\tau = 0)$ evaluated in an experimental setup is affected by the finite response time of the detectors. As a consequence, it is possible to identify single-photon source once $g^{(2)}(0) < 1/2$, with $g^{(2)}(0) = 1/2$ being the second order correlation function for two photons (see Appendix A).
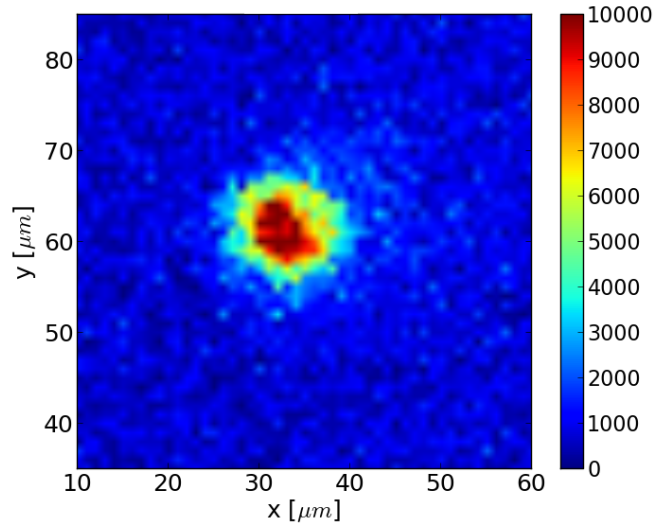
Figure 5.6: Photoluminescence image of an NV center, acquired while continuously exciting the NV center, scanning the sample with the galvanometric mirror and recording the signal with APD2.

In Figure 5.7 the measurement of the second order correlation function is presented. The fitting of the data leads to $g^{(2)}(0) = 0.27$ for the emission of the bright spot identified in Figure 5.6. This value is lower than 0.5 thus it verifies that the radiation spot is due to the emission of single-photons.

A last confirmation that the bright light spot is a NV center is provided by the photoluminescence spectrum. An emission spectrum, recorded in Figure 5.8, is therefore acquired by a spectrum analyser in the spectral range from 550 nm to 850 nm. The acquisition is performed for 15 minutes using as excitation light the 532 nm line of the continuous laser at 5 mW. In the spectrum the characteristic ZPL of NV^- at 637.2 nm and the broad PSB clearly identify the bright spot as a NV center.

In conclusion through a sequence of measurements of the galvanometric signal, the second order correlation function and the emission spectrum of a fluorescence spots it is possible to identify with success the photolumiscence emission of nitrogen-vacancy centers in nanodiamonds.
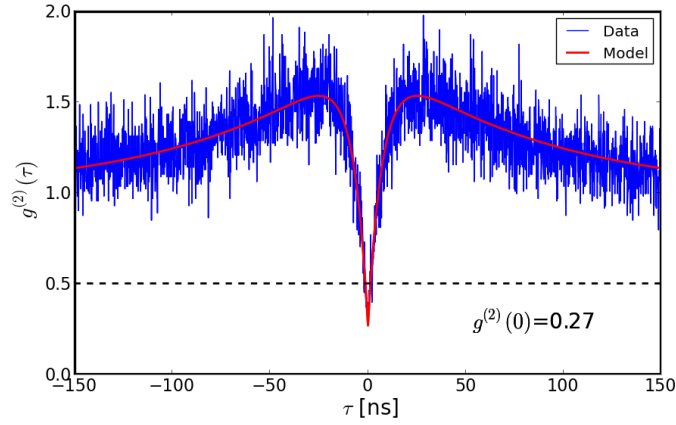
Figure 5.7: Second order correlation function $g^{(2)}(\tau)$ measurement of the NV center of Figure 5.6. Blue line represent the data collected through the Hanbury Brown and Twiss setup, while red line is the best fit to the data, resulting in $g^{(2)}(0) = 0.27$.
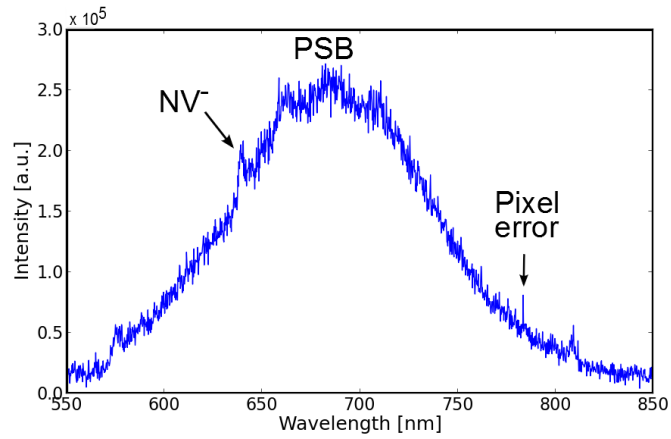
Figure 5.8: Photoluminescence of a NV center in a nanodiamonds with size < 50 nm. The spectrum is acquired for 15 minutes on the center of the bright spot in Figure 5.6. The spot is excited with a 532 nm continuous laser at 5 mW. The NV^- ZPL is clearly visible at 637.2 nm. The broad PSB peak dominates the spectrum.

Chapter 6

Conclusions

This project addresses the increasing interest for single-photon sources required for quantum information, by experimentally studying the development of a fiber Fabry-Pérot cavity (FFPC), to enhance the single-photon emission of nitrogen-vacancy (NV) centers in nanodiamonds.

The FFPC cavity is implemented starting from investigating laser-machining as a method to produce ultrasmooth concave structures on silica. A specific setup has been assembled for such task and has been used to characterize the process starting from inscribing silica plates and then moving on to the end facets of optical fibers. The scheme is based on the absorption of a 10.6 μm beam emitted by a CO_2 laser. As the beam quality is critical for producing the desired structures, the beam profile has been characterized along the full path. Additionally, to ensure stable machining, a power control system based on a thermal sensor and a set of shutters has been designed.

The machined structures of micro-metric dimensions have been measured through atomic force microscope (AFM) and the main geometrical features are extracted by the surface profilometry. A characterization performed over a systematic set of depressions imprinted on silica plates reveals the impact of the laser parameters used during the surface processing on the geometrical properties of the concave structures. However, the improved power instability of the laser attained with the designed setup enabled achieving a level of dispersion of the concave structures' features lower than 20%. This figure is comparable with state-of-the-art results reported for this technique [20].

In order to optimize the coupling between the FFPC mode and the output of the single mode fiber, numerical simulations of the cavity properties have been performed. The results concluded that concave structures with larger radii of curvature and lower depths are favorable.

A macroscopic cavity has been experimentally characterized coupling it to a laser diode and tuning the cavity length by means of a piezoelectric actuator. The measurement of its reflection spectrum allowed an estimation of the cavity finesse of about 118.2±0.5, comparable with the one

expected from its theoretical losses with a difference below 11%.

Finally a characterization of NV centers emission was performed using a scanning confocal microscope. Measurements of the second order correlation function of the emitted light proved the single-photon emission of NV centers.

In this work, the fiber facets' characterization was mainly limited by the lack of a holder for the AFM, which did not allow precise measurements of the concave structures imprinted on the fiber tips. The characterization could therefore be significantly improved by such measurements increasing the understanding on the requirements for the laser-machining setup.

Furthermore, a flowbox will be used for the laser-machining setup and it is expected to provide a cleaner environment for the surface processing thus reducing the imperfections of the inscribed structures.

Nevertheless, the promising results here outlined are being carried forward with the application of multilayer dielectric coating on the fibers at LAYERTEC Laboratories, planned for the next months. The first attempts to coherently couple the NV centers to the FFPC can be then expected for the next year. In particular, to continue with the investigation a PhD project entitled "Quantum Protocols with a Colour Centre in a Microcavity" has been started within the QPIT group, carried out by Clemens Schäfermeier under the supervision of Assist. Prof. Alexander Huck and Prof. Ulrik L. Andersen. Interesting studies are therefore ongoing at this very moment.

Appendix A

Second-order correlation function
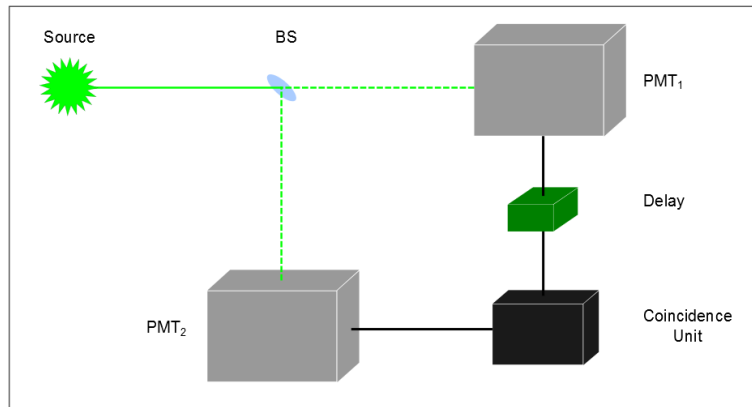
Figure A.1: Schematic representation of the experimental set-up proposed by Hanbury Brown and Twiss [58]. The light emitted by the source is split by a beamsplitter and is detected by two multipliers PMT_1 and PMT_2.

A convenient way of quantifying the quantum properties of light is according to the *second-order correlation function* $g^{(2)}(\tau)$. Through this property, light is described as *antibunched*, *coherent* or *bunched*. Antibunched light can be understood only using a photon interpretation of light, thus is strictly connected to its quantum nature. A practical application of antibunched light is in single-photon sources.

To date, the most efficient method to measure a single-photon is the measurement of the second order correlation function through the Hambury-Brown and Twiss experiment [58]. In this configuration (Figure A.1) a light beam is split through a beam splitter and then detected by two photomultipliers PMT_1 and PMT_2. In one of the two electrical paths a delay generator τ is inserted. Finally outputs of the photomultipliers reach a coincidence module.

For a source with constant average intensity, the second order correlation $g^{(2)}(\tau)$ is defined by

$$g^{(2)}(\tau) = \frac{\langle I(t)I(t+\tau)\rangle}{\langle I(t)\rangle^2} \qquad (A.1)$$

From Equation A.1, it follows that the second-order correlation function investigates the temporal coherence of the source. The time-scale of the intensity fluctuations of the source, given by the coherence time τ_C, allows defining different source types. If $\tau \gg \tau_C$ the intensity fluctuations at t and $t+\tau$ are uncorrelated to each other, therefore $g^{(2)}(\tau \gg \tau_C) = 1$. While if $\tau \ll \tau_C$ there is correlations between the two times. In particular if $\tau = 0$, the correlation function results

$$g^{(2)}(0) = \frac{\langle I(t)^2\rangle}{\langle I(t)\rangle^2} \qquad (A.2)$$

Consider a photon stream consisting of individual photons with long time intervals between them, the individual photons cannot be detect by the two detectors at the same time, thus the correlation function for single-photon results to be $g^{(2)}(0) = 0$.

The second order correlation function of anti-bunched light in a quantum state of n photons (Fock state $|n\rangle$) can be expressed analytically as:

$$g^{(2)}(\tau) = \frac{\langle n|a^\dagger(0)a^\dagger(\tau)a(\tau)a(0)|n\rangle}{\left(\langle n|a^\dagger a|n\rangle\right)^2} \qquad (A.3)$$

where a and $a^\dagger$ are the standard annihilation and creation operators defined in the second quantization of light.

In case of $\tau = 0$ Equation A.3 reduces to [60]

$$g^{(2)}(0) = \frac{n(n-1)}{n^2} \qquad (A.4)$$

As a consequence for single-photon n=1, thus ideally $g^{(2)}(0) = 0$. However, since a state with n=2 instead is characterized by $g^{(2)}(0) = 1/2$, sources exhibiting $g^{(2)}(0) < 1/2$ can be defined as single-photon sources [61].

Appendix B

LabView control program

A LabView program, implemented for this project, drives the shutters' system, the CO_2 laser, and the thermal sensor acquisition in the laser-machining setup. The program interface is shown in Figure B.1, while Figures B.2 present the LabView code.
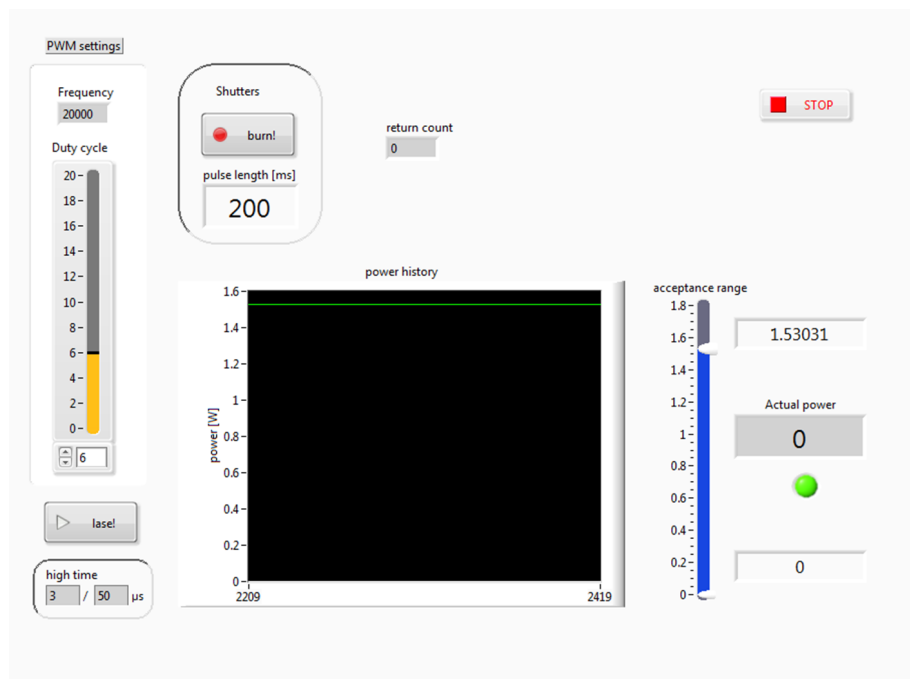
Figure B.1: LabView interface of the $C0_2$ setup driving program.
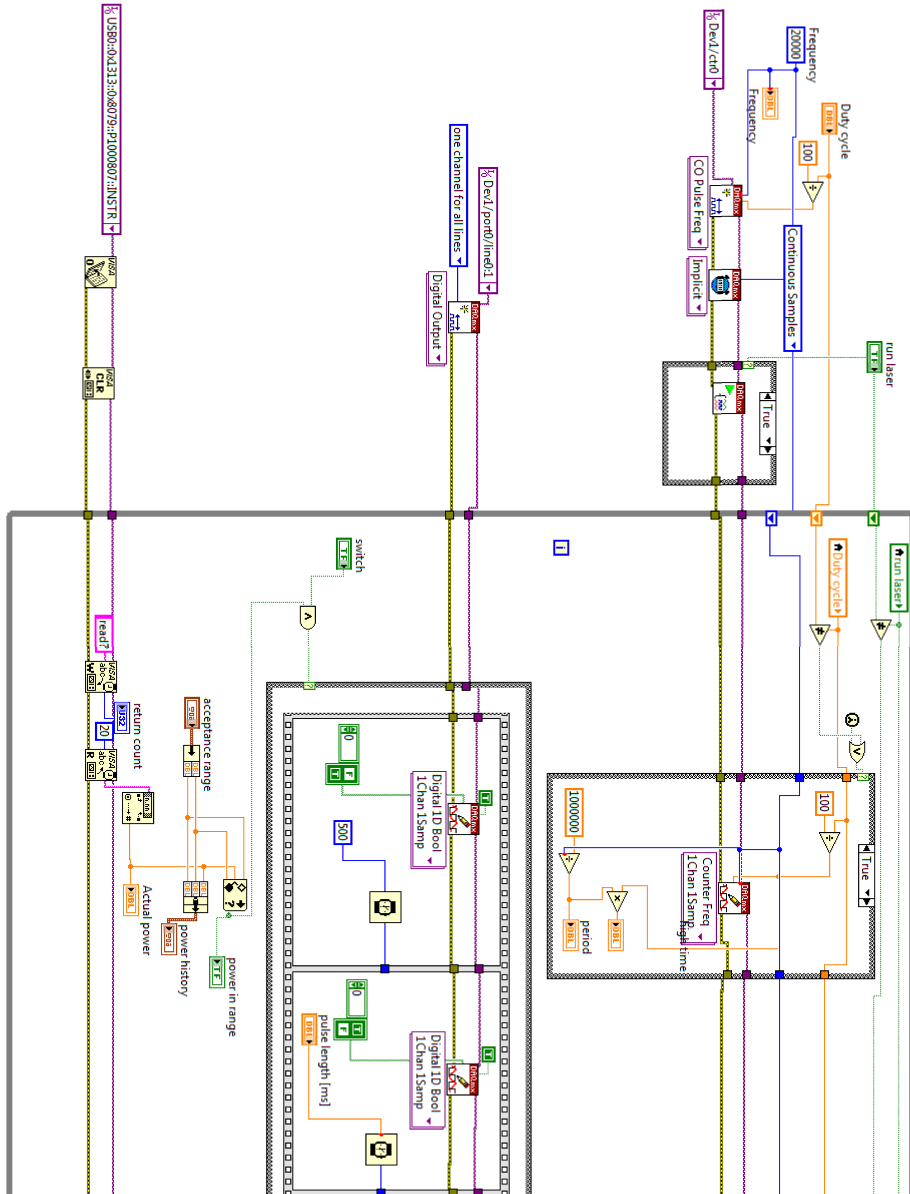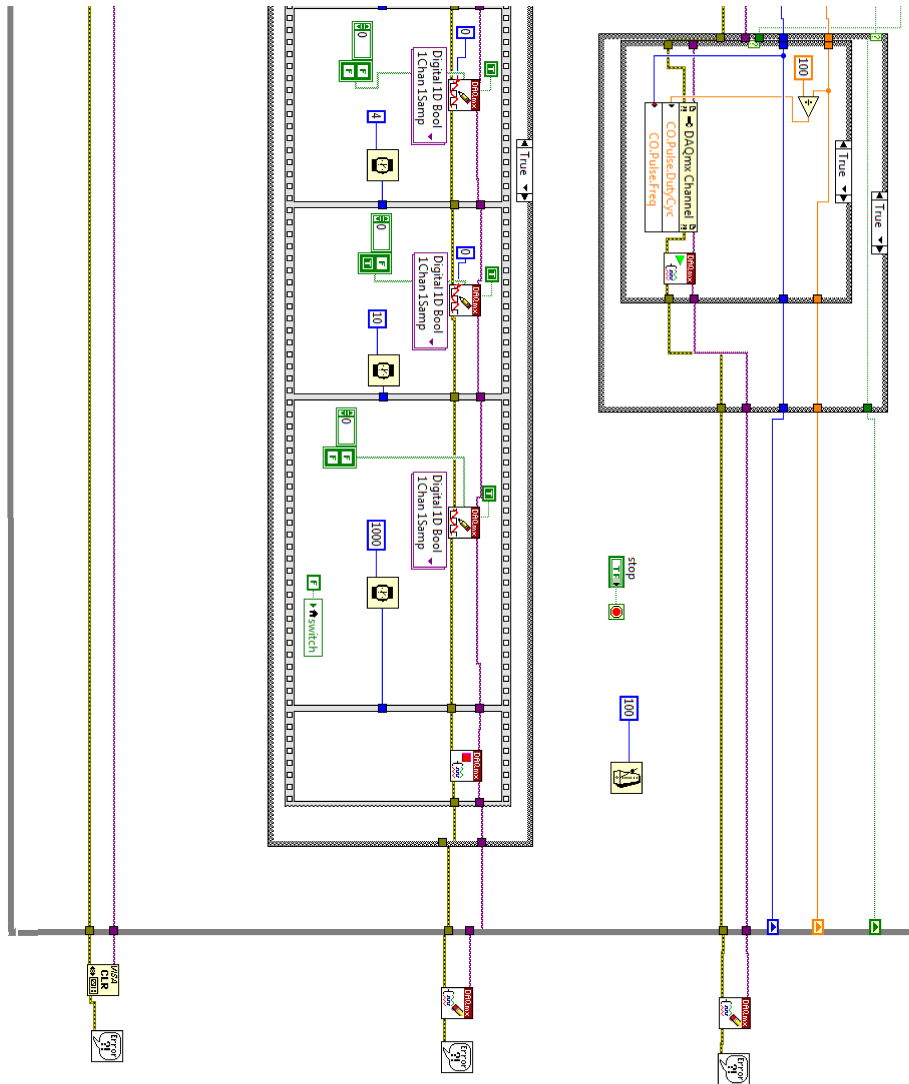
Figure B.2: LabView code of the C0$_2$ setup driving program. The block diagram on the right provides the driving signal to the CO$_2$ Firestar laser. The central block diagram combines the remote control of the shutters' system with the gating signal of the laser. Finally the block diagram on the left sets the acceptable power range and records the power sensor's measurement in a timeline chart.

Appendix C

Data analysis routine

In the following code the main functions implemented and used to analyst the concave structures are provided.

```python
"""
Concave structures' analysis
"""


from __future__ import division
from matplotlib.pyplot import *
import sys
import cPickle as pickle
from scipy.optimize import curve_fit, minimize, Result, leastsq
import os.path as osp
from numpy import *
import pdb
from mpl_toolkits.mplot3d import Axes3D
from guiqwt import tests
from guiqwt.plot import ImageDialog
from guiqwt.builder import make

filename ='holes20130605_b_17_duty_25ms.txt'
basedir= '/home/user1/'
basedir2 = '/home/user1/data-fitting/'
step_numbers= 256 #number of AFM steps for every row
```

```python
def loadfile(filename):
    """
    Read comma-separated NOVA export file with header, AFM data format.
    Add header information to self.info dictionary, raw data to
    self.data_raw, and scaled  data to self.data.
    """
    info = {'meta':''}
    fullpath = osp.join(basedir, filename)
    try:
        lines = open(fullpath).readlines()
    except IOError:
        print "File", fullpath, "not found."
        print "Please run the loadfile(filename) method."
        return
    for i, line in enumerate(lines):
        if line.startswith('Start of Data'):
            i_data = i + 1
            break
        else:
            inf = [s.strip() for s in line.split('=')]
            if len(inf) == 2:
                try:
                    info[inf[0]] = float(inf[1].replace(',', '.'))
                except ValueError:
                    info[inf[0]] = inf[1]
            else:
                info['meta'] += inf[0] + '\n'
    # read and scale data values
    Z = array([l.split() for l in lines[i_data:]], dtype='float')
    if info['Unit X'] == 'Angstrom' and info['Unit Data'] == 'nm':
        Z += info['Bias Data']
        Z *= info['Scale Data'] * .001
        x = arange(step_numbers) * info['Scale X'] * .0001
        y = arange(step_numbers) * info['Scale Y'] * .0001
        X, Y = meshgrid(x, y)
    else:
```

```
            print 'Unexpected units – data not scaled.'
        return x, y, Z


def Rotation(x,y, theta):
    """
    Make a rotation of the coordinates of an angle theta
    Input: x[array], y[array], theta
    Output: new coordinates x[array], y[array]
    """
    x=x* cos(theta)-y*sin(theta)
    y=x* sin(theta)+y*cos(theta)
    return (x,y)


def TWODGauss(x, y, B, A, x_0, xsigma, y_0, ysigma, theta=0):
    """
    Define a 2D Gaussian
    Input: x[array], y[array], Background, Amplitude[if >0, the Gaussian
    is for (y-B)<0], x0, xsigma, y0, ysigma, theta[ default=0 else it
    implies a  rotation of the axis]
    Output:2D Gaussian
    """
    x,y=Rotation(x,y,theta)
    return (B- A * exp(-((x-x_0)**2/(2*xsigma**2) + (y-y_0)**2/(2*ysigma**2))))


def PLANE(x,y, A, B, C):
    """
    Define a Plane
    Input: x[array], y[array], A, B, Background
    Output: Plane
    """
    return (A*x+B*y+C)


def FFT_analysis(x,y,Z, pixel):
    """
    Fast Fourier Transform and low-pass filter to compensate
    for cantilever noise.
```

```python
    Input: x[array], y[array], Z[matrix],pixel[number of pixel
    to collect along the x axis in the Fourier space]
    Output:2D Gaussian
    """
    freq=fft.fftfreq(step_numbers, x[1]-x[0])
    rec_x_axis=r_[freq[step_numbers/2:], freq[:step_numbers/2]]
    rec_y_axis=r_[freq[step_numbers/2:], freq[:step_numbers/2]]
    S=fft.fftn(Z)
#     rearrange the quadrants
    S1 = r_[S[step_numbers/2:], S[:step_numbers/2]]
    S1 =  c_[S1[:,step_numbers/2:], S1[:,:step_numbers/2]]
#      definition of the box for the correction and correction
    box=ones((step_numbers,step_numbers))
    box[139:step_numbers,(step_numbers/2-pixel):(step_numbers/2+1+pixel)]=0
    box[0:117,(step_numbers/2-pixel):(step_numbers/2+1+pixel)]=0
    S2_box=S1*box
#     rearrange the quadrants
    S2=c_[S2_box[:,step_numbers/2:], S2_box[:,:step_numbers/2]]
    S2= r_[S2[step_numbers/2:], S2[:step_numbers/2]]
    Z1=(fft.ifftn(S2)).real
    S2=S1*TWODGauss(rec_y_axis, rec_x_axis,0,100, 0.7, 0.1, 0, 0.05)
    figure()
    contourf(rec_x_axis, rec_y_axis, log(abs(S2)**2))
    colorbar()
    return (Z1)


def FFT_analysis_noise(x,y,Z, g_width):
    """
    Fast Fourier Transform and high-pass filter to estimate the cantilever noise.
    Input: x[array], y[array], Z[matrix],pixel[number of pixel to collect
    along the x axis in the Fourier space]
    Output:2D Gaussian
    """
    freq=fft.fftfreq(step_numbers, x[0][0]-x[0][1])
    rec_x_axis=r_[freq[step_numbers/2:], freq[:step_numbers/2]]
    rec_y_axis=r_[freq[step_numbers/2:], freq[:step_numbers/2]]
```

```
    S=fft.fftn(Z)
    REC_X_AXIS,REC_Y_AXIS=meshgrid(rec_x_axis, rec_y_axis)


#      rearrange the quadrants
    S1 = r_[S[step_numbers/2:], S[:step_numbers/2]]
    S1 =  c_[S1[:,step_numbers/2:], S1[:,:step_numbers/2]]
    gauss=lambda x, y, width:1-exp(-(x**2+y**2)/(2*width**2))
    S2_box=S1*gauss(REC_X_AXIS,REC_Y_AXIS, g_width)
#      rearrange the quadrants
    S2=c_[S2_box[:,step_numbers/2:], S2_box[:,:step_numbers/2]]
    S2= r_[S2[step_numbers/2:], S2[:step_numbers/2]]
    Z1=(fft.ifftn(S2)).real
    return (Z1)


def Chosen_region(X,Y,Z, Z0, depth,cut=2/3):
    """
    Reduce the area for the fitting at the lowest 1/3 of the structure
    Input: x[matrix], y[matrix], Z[matrix],Z0[background],
    depth [of the Gaussian], cut[upper part of the Gaussian negleted]
    Output:x[flat array], y[flat array], Z[flat array]
    """
    Z_=Z.flatten()
    Z_index=Z_<=(Z0+cut*depth)
    X_=(X.flatten())[Z_index]
    Y_=((Y).flatten())[Z_index]
    Z_=Z_[Z_index]
    return (X_,Y_,Z_)


def TWOD_fitting_AFM(filename, pixel=0, rot=False, cut=2/3, roundtop=True):
    """
    Fitting of the AFM scan output with a 2D Gaussian, using a Fourier
    Analysis filter along the direction of the scan, considering the
    lowest 1/3 of the hole (1-cut).
    Input= filename, pixel[number of pixel for the Fourier Analysis filtering -1],
           Rot[if True it makes a rotation of the coordinates for the fitting],
           cut[upper part of the Gaussian negleted]
```

```python
    Output=X[matrix], Y[matrix], Z[matrix], Fitting result
    Fitting result[0]=Parameters= Background, Amplitude[if >0, the Gaussian
                    is for (y-B)<0],x0, xsigma, y0, ysigma, theta[rotation
                    of the Gaussian, given only if rot=True]
    Fitting result[1]=Cov_
    """
    x,y,Z = loadfile(filename)
    Z=FFT_analysis(x,y,Z, pixel)
    X, Y = meshgrid(x, y)
# parameter guesses
    if roundtop: Z0=mean((sort(Z.flatten()))[-1000:-1])
    else:
        base= r_[arange (0,15), arange (step_numbers-15,step_numbers)]
        BASE,BASE=meshgrid(base,base)
        Z0= mean(Z[BASE,BASE])
    depth=-abs(Z0-Z.min())
    x0_guess=X[Z==Z.min()][0]
    y0_guess=Y[Z==Z.min()][0]
    sigma_x_guess=abs(x0_guess-mean(x[(Z[y==y0_guess,:]==min(Z[y==y0_guess,
    ((Z[y==y0_guess,:])>=(Z0+2/3*depth))[0]]))[0]]))
    sigma_y_guess=abs(y0_guess-mean(y[((Z[:,x==x0_guess]==min(Z[(((Z[:,
    x==x0_guess])>=(Z0+2/3*depth)).T)[0],x==x0_guess])).T)[0]]))
    theta_guess=0
    X_,Y_,Z_=Chosen_region(X,Y,Z,Z0,cut,depth)
 # fitting
    residual_2=lambda P: (Z_-TWODGauss(X_,Y_, *P[:(7 if rot else 6)]))#.flatten()
    guess=[Z0, depth, x0_guess,sigma_x_guess, y0_guess, sigma_y_guess,
          theta_guess][:(7 if rot else 6)]
    Fitting_Gauss= leastsq(residual_2,guess,full_output=1)
    return(X,Y,Z, Fitting_Gauss)


def cantilever_noise_FIT(X,Y,Z, width=15):
    Z=FFT_analysis_noise(X,Y,Z, width)
    Z_= Z.flatten()
    X_= X.flatten()
    Y_= Y.flatten()
```

```
    residual_2=lambda P:(Z_-PLANE(X_,Y_, *P))
    guess=[1,2,0.1]
    Fitting_Plane=leastsq(residual_2, guess,full_output=True)
    residual_3=lambda P: ((Z_-PLANE(X_,Y_, *P))**2).sum()# reduce area for RMS
    RMS=sqrt(mean(residual_3(Fitting_Plane[0]))/len(X))
    return (RMS, X,Y,Z, Fitting_Plane)


def ThreeD_PLT_FIT(filename, roundtop, rot=False):
    """
    3D rapresentation of the fitting curve, with a 2D Gaussian,
    and the data collected with the AFM
    """
    X,Y, Z, Fitting_Gauss= TWOD_fitting_AFM(filename, rot)
    fig =plt.figure(figsize=(10,6))
    ax = fig.add_subplot(111, projection='3d')
    ax.view_init(-15, 30)
    ax.set_xlabel(r'[$\mu m$]')
    ax.set_ylabel(r'[$\mu m$]')
    ax.set_zlabel(r'[$\mu m$]')
    ax.plot_surface(X, Y, Z, cmap=cm.coolwarm)
    ax.plot_wireframe(X, Y,TWODGauss(X, Y, *Fitting_Gauss[0]), rstride=10,
    cstride=10)#Res[0],Res[1],Res[2],Res[3],Res[4],Res[5]
    ax.set_zlim(-4, 0.5)
    return fig


def ThreeD_PLT_noise(filename):
    """
    3D rapresentation of the fitting curve, with a 2D Gaussian,
    and the data collected with the AFM
    """
    x,y,Z=loadfile(filename)
    X, Y = meshgrid(x, y)
    RMS, X,Y,Z, Fitting_Plane= cantilever_noise_FIT(X,Y,Z,3)
    print 'a'
    fig = plt.figure()
    ax = fig.add_subplot(111, projection='3d')
```

```python
    ax.view_init(30, -15)
    ax.plot_surface(X, Y, Z, cmap=cm.Reds)
    ax.plot_wireframe(X, Y,PLANE(X, Y, *Fitting_Plane[0]), rstride=1,
    cstride=1)#Res[0],Res[1],Res[2],Res[3],Res[4],Res[5]
    return fig, RMS


def TwoD_PLT_FIT(filename, rot=False):
    """
    Projection in 2D of the fitting curve  with a 2D Gaussian
    and the data collected with the AFM
    """
    X,Y, Z, Fitting_Gauss= TWOD_fitting_AFM(filename, rot)
    Param=Fitting_Gauss[0]
    Gauss_1D=lambda x,B,A, x0, sigma_x: (B- A*exp(-(x-x0)**2/(2*sigma_x**2)))
    Y_0=Y[Z==Z.min()]
    plot(X[0], Gauss_1D(X[0], *Param[:4]))
    plot(X[0], Z[:][Y==Y_0], 'o')
    ax = fig.add_subplot(111, projection='3d')
    ax.plot_surface(X, Y, Z, cmap=cm.coolwarm)
    ax.plot_wireframe(X, Y,TWODGauss(X, Y, *Fitting_Gauss[0]), rstride=10,
    cstride=10)
    return()


def ROC_calculus(Parameters, Covariance):
    """
    Given the result of the TWODGauss_fitting it calculates the radius of
    curvature as the width squared normalized by the amplitude of the Gaussian.
    Input = TWODGauss_fitting[3][0], TWODGauss_fitting[3][1]
    Output= ROC_x, ROC_x_err, ROC_y, ROC_y_err
    """
    ROC_x=(Parameters[3]**2/Parameters[1])
    ROC_x_err=ROC_x*sqrt((2*Covariance[3][3]**0.5/Parameters[3])**2+
    (Covariance[1][1]**0.5/Parameters[1])**2)
    ROC_y=(Parameters[5]**2/Parameters[1])
    ROC_y_err=ROC_y*sqrt((2*Covariance[5][5]**0.5/Parameters[5])**2+
    (Covariance[1][1]**0.5/Parameters[1])**2)
```

```python
    return [ROC_x, ROC_x_err, ROC_y, ROC_y_err]


def RMS_calculus(X, Y, Z, Parameters):
    """
    Given the result of the TWODGauss_fitting it calculates the RMS as an
    estimation of the surface roughness
    Input = X,Y,Z,TWODGauss_fitting[3][0]
    Output= RMS
    """
    residual_2=lambda P: ((Z-TWODGauss(X,Y,*P))**2).sum()
    RMS=sqrt( (residual_2(Parameters))/len(X))
    return (RMS)


def create_window():
    win = ImageDialog(edit=False, toolbar=True, wintitle="Cross sections test",
                      options=dict(show_xsection=True, show_ysection=True))
    win.resize(600, 600)
    return win


def AFM_structure_analysis(filename, rot=False, plt_3d=False, plt_2d=False,
return_full=False, roundtop=False, savefigure=False):
    """
    Analysis of the AFM scans of the structures.
    Input: filename
           rot[ if True a rotational angle around z is inserted in the
           extimated parameters],
           plt_3d [if true provide the 3D rapresentation of the fitting
           curve and the data]
           plt_2d [if true provide the 2D rapresentation of the fitting
           curve and the data]
    Output:[Depth, Depth_err], [ROC_x, ROC_x_err, ROC_y, ROC_y_err],
            depth[guess of the depth]
            if return_full=True
                   [[Depth, Depth_err], [W_x, W_x_err,W_y,W_y_err],
                   [ROC_x, ROC_x_err, ROC_y, ROC_y_err], RMS, depth]
    """
```

```
    global Chosen_reg, Parameters
    X,Y,Z, Fitting_result=TWOD_fitting_AFM(filename, roundtop)
    Parameters=Fitting_result[0]
    Cov_x=Fitting_result[1]
    m=len(Parameters)
    cut=2/3
    if roundtop: Z0=mean((sort(Z.flatten()))[-1000:-1])
    else:
        base= r_[arange (0,15), arange (step_numbers-15,step_numbers)]
        BASE,BASE=meshgrid(base,base)
        Z0= mean(Z[BASE,BASE])
#       selection of the fitted region
    depth=-abs(Z0-Z.min())
    Chosen_reg=Chosen_region(X,Y,Z,Z0,depth, cut)
    n=size(Chosen_reg[0])
    Covariance_matrix= Cov_x*((Chosen_reg[2]-TWODGauss(Chosen_reg[0],
    Chosen_reg[1], *Parameters))**2).sum()/(n-m)
    Depth= Parameters[1]
    Depth_err=sqrt(Covariance_matrix[1][1])
    W_x=Parameters[3]
    W_x_err=sqrt(Covariance_matrix[3][3])
    W_y=Parameters[5]
    W_y_err=sqrt(Covariance_matrix[5][5])
    ROC_x, ROC_x_err, ROC_y, ROC_y_err= ROC_calculus(Parameters, Covariance_matrix)
    RMS=RMS_calculus(Chosen_reg[0], Chosen_reg[1], Chosen_reg[2], Parameters)
    if plt_3d : ThreeD_PLT_FIT(filename, rot)
    if plt_2d : fit_test(X,Y,Z, Parameters)
    if savefigure:
        fig=ThreeD_PLT_FIT(filename, roundtop, rot)
        fig.savefig(filename+'_b.png')
    if return_full:
        return [[Depth, Depth_err], [W_x, W_x_err,W_y,W_y_err], [ROC_x, ROC_x_err,
        ROC_y, ROC_y_err], RMS, depth]
    else:
        return [[Depth, Depth_err], [ROC_x, ROC_x_err, ROC_y, ROC_y_err], depth]
```

```python
def Test_FFT():
    """
    It provides an estimation of the RMS as a function of the number of
    pixel used for the FFT filtering
    """
    step=1
    pixels=range(0,step_numbers/2,step)
    posx=step_numbers/2
    posy=171
    file = open('FFT_RMS.txt', 'w')
    x,y,Z = loadfile(filename)
    X, Y = meshgrid(x, y)
    file.write('0,      0.004364 \n')
    base= r_[arange (0,15), arange (step_numbers-15,step_numbers)]
    BASE,BASE=meshgrid(base,base)
    Z0=mean((sort(Z.flatten()))[-1000:-1])
    depth=-abs(Z0-Z.min())
    for i in pixels:
        X,Y,Z__,Par=TWOD_fitting_AFM(filename, pixel=i)
        pix=1+2.*i
        figure('hor, %d' %pix)
        plot(x, Z[posx,:],x,Z__[posx,:], x, TWODGauss(X,Y,*(Par[0]))[posx,:])
        xlabel(r'x[$\mu m$]')
        ylabel(r'z[$\mu m$]')
        savefig('hor, pixels=%d, position=%.f' %(pix, posx))
        figure('vert, %d' %pix)
        plot(x, Z[:,posy],x,Z__[:,posy], x, TWODGauss(X,Y,*(Par[0]))[:,posy])
        xlabel(r'x[$\mu m$]')
        ylabel(r'z[$\mu m$]')
        savefig('vert,pixels=%d, position=%.f' %(pix, posy))
        Chosen_reg=Chosen_region(X,Y,Z__,Z0,depth)
        RMS=RMS_calculus(Chosen_reg[0],Chosen_reg[1],Chosen_reg[2], Par[0])
        file.write('%.d,      %.6f \n' %(pix, RMS))
    file.close()
    close('all')
    return()
```

Acronyms

AFM atomic force microscope

APD avalanche photo diode

BS beam splitter

CCD charge-coupled device

FFPC fiber Fabry-Pérot cavity

FSR free spectral range

FWHM full width at half maximum

HWP half waveplate

NV nitrogen-vacancy

MM multi-mode

PSB phonon-side band

PWM pulse-width modulation

PVA polyvinyl alcohol

PZT lead zirconate titanate

rpm revolutions per minutes

RMS residual mean square

ROC radius of curvature

SM single-mode

TAC time to amplitude converter

TEM transverse electric magnetic

TTL transistor-transistor logic

VCA voice coil actuator

ZPL zero phonon line

Bibliography

[1] R. Feynman, "Simulating physics with computers", *Int. J. Theor. Phys.*, **21** (6):467-488 (1982), doi: 10.1007/BF02650179.

[2] D. Deutsch, "Quantum theory, the church-turing principle of the universal quantum computer.", *Proc. R. Soc. Lond., A*, **400** pp. 97-117 (1985), doi:10.1098/rspa.1985.0070.

[3] B. Lounis and M. Orrit , "Single-photon sources.", *Rep. Prog. Phys.* **68** 1129 (2005), doi:10.1088/0034-4885/68/5/R04.

[4] R. Blatt and D. J. Wineland, "Entangled states of trapped atomic ions.", *Nature* **453** (7198): 1008–1014 (2008), doi:10.1038/nature07125.

[5] E.L. Raab, M. Prentiss, A. Cable, S. Chu, and D.E. Pritchard, "Trapping of neutral sodium atoms with radiation pressure.", *Phys. Rev. Lett.* **59** 2631–2634 (1987), doi:10.1103/PhysRevLett.59.2631.

[6] H. Mabuchi, J. Ye, and H.J. Kimble, "Full observation of single-atom dynamics in cavity QED.", *Appl. Phys. B-Lasers O* **68** (6):1095-1108 (1999), doi:0.1007/s003409901467.

[7] P. Munstermann, T. Fischer, P. Maunz, P.W.H. Pinkse, and G. Rempe, "Dynamics of single-atom motion observed in a high-finesse cavity.", *Phys. Rev. Lett.* **82** 3791-3794 (1999), doi:10.1103/PhysRevLett.82.3791.

[8] J. McKeever, A. Boca, A.D. Boozer, R. Miller, J.R. Buck, A. Kuzmich, and H.J. Kimble, "Deterministic generation of single photons from one atom trapped in a cavity.", *Science* **303** 5666: 1992-1994 (2004), doi:10.1126/science.1095232.

[9] J. Ye, H.J. Kimble, and H. Katori, "Quantum State Engineering and Precision Metrology Using State-Insensitive Light Traps.", *Science* **320** 5884: 1734-1738 (2008), doi:10.1126/science.1148259.

[10] C.C. Nshii, M. Vangeleyn, J.P. Cotter, P.F. Griffin, E.A. Hinds, C.N. Ironside, P. See, A.G. Sinclair, E. Riis, and A.S. Arnold, "A surface-patterned chip as a strong source of ultracold atoms for quantum technologies", *Nat. Nanotechnol.* **8** 321–324 (2013), doi:10.1038/NNANO.2013.47.

[11] A. Gruber, A. Dräbenstedt, C. Tietz, L. Fleury, J. Wrachtrup, and C. von Borczyskowski, "Scanning Confocal Optical Microscopy and Magnetic Resonance on Single Defect Centers", *Science*, **276** (5321): 2012-2014 (1997), doi:10.1126/science.276.5321.2012.

[12] E. Togan, Y. Chu, A.S. Trifonov, L. Jiang, J. Maze, L. Childress, M.V.G. Dutt, A.S. Sørensen, P.R. Hemmer, A.S. Zibrov, and M.D. Lukin, "Quantum entanglement between an optical photon and a solid-state spin qubit.", *Nature* **466** 730–734 (2010), doi:10.1038/nature09256.

[13] G. Balasubramanian, P. Neumann, D. Twitchen, M. Markham, R. Kolesov, N. Mizuochi, J. Isoya, J. Achard, J. Beck, J. Tissler, V. Jacques, P.R. Hemmer, F. Jelezko, and J. Wrachtrup, "Ultralong spin coherence time in isotopically engineered diamond.", *Nat. Mat.* **8** 383 (2009), doi :10.1038/nmat2420.

[14] L. Childress, J. M. Taylor, A.S. Sorensen, and M.D. Lukin, "Fault-Tolerant Quantum Communication Based on Solid-State Photon Emitters", *Phys. Rev. Lett.* **96** 070504 (2006), doi:10.1103/PhysRevLett.96.070504.

[15] G. Balasubramanian, I.Y. Chan, R. Kolesov, M. Al-Hmoud, J. Tisler, C. Shin, C. Kim, A. Wojcik, P.R. Hemmer, A. Krueger, T. Hanke, A. Leitenstorfer, R. Bratschitsch, F. Jelezko, and J. Wrachtrup, "Nanoscale imaging magnetometry with diamond spins under ambient conditions", *Nature* **455** 648-651 (2008), doi:10.1038/nature07278.

[16] A. Faraon, P.E. Barclay, C. Santori, K.-M.C. Fu, and R.G. Beausoleil, "Resonant enhancement of the zero-phonon emission from a colour centre in a diamond cavity", *Nat. Photonics* **5** 301–305 (2011), doi:10.1038/nphoton.2011.52.

[17] T. Steinmetz, Y. Colombe, D. Hunger, T.W. Hänsch, A. Balocchi, R.J.Warburton, and J. Reichel, "Stable fiber-based Fabry-Pérot cavity", *Appl. Phys. Lett.*, **89** 111110 (2006), doi:10.1063/1.2347892.

[18] A. Huck, S. Kumar, A. Shakoor, and U.L. Andersen, "Controlled Coupling of a Single Nitrogen-Vacancy Center to a Silver Nanowire", *Phys. Rev. Lett.*, **106**, 096801 (2011), doi:10.110/PhysRevLett.106.096801.

[19] D. Hunger, T. Steinmetz, Y. Colombe, C. Deutsch, T. W. Hänsch, and J. Reichel,"A fiber Fabry–Pérot cavity with high finesse. New Journal of Physics", *New J. Phys.*, **12** 065038 (2010), doi:10.1088/1367-2630/12/6/065038.

[20] D. Hunger, C. Deutsch, R. J. Barbour, R. J. Warburton, and J. Reichel, "Laser micro-fabrication of concave, low roughness features in silica", *AIP Advances*, **2** 012119 (2012), doi:10.1063/1.3679721.

[21] F.L. Pedrotti and L.S. Pedrotti, *Introduction to Optics*, Prentice Hall International (1987).

[22] P.W. Milonni and J.H. Eberly, *Laser Physics*, John Wiley and Sons (2010).

[23] W.T. Silfvast, *Laser Fundamental*, Cambridge University Press (2004).

[24] A.E. Siegman, *Lasers*, University Science Books (1986).

[25] M. Fox, *Quantum Optics, An Introduction*, Oxford University Press (2006).

[26] L. Salasnich, *Quantum Physics of Light and Matter*, Springer (2014)

[27] J.M. Bennett, "Recent developments in surface roughness characterization", *Meas. Sci. Technol*, **3** 1119 (1992), doi:10.1088/0957-0233/3/12/001.

[28] C. Deutsch, "High finesse fibre Fabry-Pérot resonators. Production, characterization and applications.", Diploma Thesis, LMU, München (2008).

[29] W.B. Joyce and B.C. DeLoach, "Alignment of Gaussian beams", *Appl. Opt.*, **23** 4187 (1984), doi:10.1364/AO.23.004187.

[30] H. Tanji-Suzuki, I.D. Leroux, M.H. Schleier-Smith, M. Cetina, A.T. Grier, J. Simon, and V. Vuletic, "Interaction between Atomic Ensembles and Optical Resonators: Classical Description", *Adv. At. Mol. Opt. Phys.* **60**, 201 (2011), doi:10.1016/B978-0-12-385508-4.00004-8.

[31] J.E. Field, *The Properties of Natural and Synthetic Diamond*, Academic Press (1992).

[32] N. Bar-Gill, "Suppression of spin-bath dynamics for improved coherence of multi-spin-qubit systems", *Nat. Comm.*, **3**, 858 (2012), doi:10.1038/ncomms1856.

[33] M.W. Doherty, N.B. Manson, P. Delaney, F. Jelezko, J. Wrachtrupe, and L. C.L. Hollenberg, "The nitrogen-vacancy colour centre in diamond", *Phys. Rep.*, **528** (2013), doi:10.1016/j.physrep.2013.02.001.

[34] C. Kurtsiefer, S. Mayer, P. Zarda, and H. Weinfurter, "Stable Solid-State Source of Single Photons", *Phys. Rev. Lett.*, **85** 290 (2000), doi:10.1103/PhysRevLett.85.290.

[35] F. Jelezko, and J. Wrachtrup, "Single defect centres in diamond: A review", *Phys. Stat. Sol. (a)*, **203** 3207 (2006), doi:10.1002/pssa.200671403.

[36] G. Davies, S. C. Lawson, A. T. Collins, A. Mainwood, and S. J. Sharp, "Vacancy-related centers in diamonds", *Phys. Rev. B*, **46** 13157 (1992), doi:10.1103/PhysRevB.46.13157.

[37] M.D. Feit and A.M. Rubenchik, "Mechanisms of CO2 laser mitigation of laser damage growth in fused silica", *Proc. SPIE*, **91** 4932 (2003), doi:10.1117/12.472049.

[38] P. Bouchut, D. Decruppe, and L. Delrive, "Fused silica thermal conductivity dispersion at high temperature", *J. Appl. Phys.*, **96** 3221 (2004), doi:10.1063/1.1776629.

[39] R. Kitamura, L. Pilon, and M. Jonasz, "Optical constants of silica glass from extreme ultraviolet to far infrared at near room temperature", *Appl. Opt.*, **46(33)** 8118 (2007). doi:10.1364/AO.46.008118

[40] M. von Allmen and A. Blatter, *Laser-Beam Interaction with Materials*, Springer (1995)

[41] W.W. Duley, *CO_2 Lasers, Effects and Applications*, Academic Press (1976).

[42] Synrad Firestar v40 operation manual, 3.1 edition, September 2010.

[43] Thorlabs V21 Photonics Catalogs, 2011.

[44] L.P. Maguire, S. Szilagyi, and R.E. Scholten, "High performance laser shutter using a hard disk drive voice-coil actuator", *Rev. Sci. Instrum.*, **75**, 3077 (2004), doi:10.1063/1.1786331.

[45] R.E.Scholten, "Enhanced laser shutter using a hard disk drive rotatory voice-coil actuator", *Rev. Sci. Instrum.*, **78** 026101 (2007), doi:10.1063/1.2437199.

[46] G. Binnig, C.F. Quate, and C. Gerber, "Atomic Force Microscope", *Phys. Rev. Lett.*, **56**, 930 (1985), doi:10.1103/PhysRevLett.56.930.

[47] R. Garcia and R. Pérez, "Dynamic atomic force microscopy methods", *Surf. Sci. Rep.*, **47** 197–301 (2002), doi:10.1016/S0167-5729(02)00077-8.

[48] R.G. Winkler, J.P. Spatz, S. Sheiko, M. Möller, P. Reineker, O. Marti, "Imaging material properties by resonant tapping-force microscopy: A model investigation", *Phys. Rev. B*, **54** 8908 (1996), doi:10.1103/PhysRevB.54.8908.

[49] A.M. Baro, R.G. Reifenberger, *Atomic Force Microscopy in Liquid: Biological Applications*, John Wiley and Sons (2012)

[50] R. Albrecht, A. Bommer, C. Deutsch, J. Reichel, and C. Becher, "Coupling of a single NV-center in diamond to a fiber-based microcavity", *Phys. Rev. Lett.*, **110**, 243602 (2013), doi:10.1103/PhysRevLett.110.243602.

[51] K.M. Nowak, H.J. Baker, and D.R. Hall, "Efficient laser polishing of silica micro-optic components",*Appl. Opt.*, **45** 000162 (2006), doi:10.1364/AO.45.000162.

[52] C.J. Hood and H.J. Kimble, "Characterization of high-finesse mirrors: Loss, phase shifts, and mode structure in an optical cavity", *Phys. Rev. A* **64** 033804 (2001), doi: 10.1103/PhysRevA.64.033804.

[53] V. Annovazzi-Lodi, S. Donati, S. Merlo, L. Zucchelli, and F. Martinez, "Protecting a power-laser diode from retroreflections by means of a fiber λ/4 retarder", *IEEE Photon. Techn. Lett.*, vol.8, no.9, pp.1278,(1996), doi: 10.1109/LPT.1996.531863.

[54] T.C. Briles, D.C. Yost, A. Cingöz, J. Ye, T.R. Schibli, and A. Cing. "Simple piezoelectric-actuated mirror with 180 kHz servo bandwidth", *Opt. Expr.*, **18**(10) 9739–46 (2010), doi:10.1364/OE.18.009739.

[55] S. Stapfner, I. Favero, D. Hunger, P. Paulitschke, J. Reichel, K. Karrai, and E.M. Weig, "Cavity nano-optomechanics: a nanomechanical system in a high finesse optical cavity", *Proc. SPIE* **7727** 06, (2010), doi:10.1117/12.854066.

[56] S. Kumar, A. Huck, and U.L. Andersen, "Efficient Coupling of a Single Diamond Color Center to Propagating Plasmonic Gap Modes", *Nano Lett.*, **13** (3) pp 1221–1225 (2013), doi: 10.1021/nl304682r.

[57] P. Xi, Y. Liu, and Q. Ren, "Scanning and Image Reconstruction Techniques in Confocal Laser Scanning Microscopy", Book Chapter in "Laser Scanning, Theory and Applications", Prof. Chau-Chang Wang (Ed.), ISBN: 978-953-307-205-0 Intech (2011).

[58] R. Hanbury Brown R. Q. Twiss, "Correlation between Photons in two Coherent Beams of Light", *Nature 177*, **27** (1956), doi:10.1038/177027a0.

[59] S. Morimune, M. Kotera, T. Nishino, K. Goto, and K. Hata, "Poly(vinyl alcohol) Nanocomposites with Nanodiamond", *Macromolecules*, **44** (11), pp 4415–4421 (2011), doi: 10.1021/ma200176r.

[60] D. Fattal, "Single photons for quantum information", Doctoral dissertation, Stanford University, (2010).

[61] L.J. Bissell, "Experimental Realization of Efficient, Room Temperature Single-Photon Sources with Definite Circular and Linear Polarizations", Doctoral dissertation, University of Rochester, (2011).